Molecular and organizational diversity intersect to generate functional synaptic heterogeneity within and between excitatory neuronal subtypes

Medeiros, A. T.[1], Gratz, S.J.[2*], Delgado, A.[2], Ritt, J.T.[2,3] and Kate M. O'Connor-Giles[1-3*]

[1] Neuroscience Graduate Training Program, Brown University, Providence, RI

[2] Department of Neuroscience, Brown University, Providence, RI

[3] Carney Institute for Brain Science, Brown University, Providence, RI

*For correspondence: Scott J. Gratz 185 Meeting St., Providence, RI 02912. email: scott_gratz@brown.edu; Kate M. O'Connor-Giles, 185 Meeting St., Providence, RI 02912. email: kate_oconnor-giles@brown.edu

The authors declare no competing interests.

ABSTRACT

Synaptic heterogeneity is a hallmark of complex nervous systems that enables reliable and responsive communication in neural circuits. In this study, we investigated the contributions of voltage-gated calcium channels (VGCCs) to synaptic heterogeneity at two closely related *Drosophila* glutamatergic motor neurons, one low- and one high-P_r. We find that VGCC levels are highly predictive of heterogeneous release probability among individual active zones (AZs) of low- or high-P_r inputs, but not between neuronal subtypes. Underlying organizational differences in the AZ cytomatrix, VGCC composition, and a more compact arrangement of VGCCs alter the relationship between VGCC levels and P_r at AZs of low- vs. high -P_r inputs, explaining this apparent paradox. We further find that the CAST/ELKS AZ scaffolding protein Bruchpilot differentially regulates VGCC levels at low- and high-P_r AZs following acute glutamate receptor inhibition, indicating that synapse-specific organization also impacts adaptive plasticity. These findings reveal intersecting levels of molecular and spatial diversity with context-specific effects on heterogeneity in synaptic strength and plasticity.

INTRODUCTION

The ability of neural circuits to effectively detect and dynamically respond to a broad range of inputs depends on a diversity of neuronal subtypes communicating through synapses with distinct properties. Neurotransmission occurs at specialized membranes called active zones (AZs) where action potentials drive the opening of voltage-gated Ca^{2+} channels (VGCCs) to trigger Ca^{2+}-dependent synaptic vesicle (SV) fusion and neurotransmitter release. Neurotransmitter release properties are determined locally at individual synapses and vary considerably both between neuronal subtypes and within homogeneous populations of neurons (Ariel et al., 2012; Atwood and Karunanithi, 2002; Branco and Staras, 2009; Hatt and Smith, 1976). In fact, functional imaging studies in *Drosophila* demonstrate that even single neurons forming synapses with the same postsynaptic partner display heterogeneous synaptic strength among individual AZs (Guerrero et al., 2005; Melom et al., 2013; Peled and Isacoff, 2011).

Presynaptic strength is defined as the likelihood of neurotransmitter release following an action potential (probability of release, P_r). This stochastic process is determined by the number of functional SV release sites and their individual probability of vesicle release. The probability of SV release is highly dependent on transient increases in intracellular Ca^{2+} levels at vesicular sensors. Accordingly, SV release sites and VGCCs are key substrates for synaptic diversity (Akbergenova et al., 2018; Aldahabi et al., 2022; Chen et al., 2015; Fedchyshyn and Wang, 2005; Fekete et al., 2019; Gratz et al., 2019; Holderith et al., 2012; Laghaei et al., 2018; Nakamura et al., 2015; Newman et al., 2022; Rebola et al., 2019; Reddy-Alla et al., 2017; Sauvola et al., 2021; Sheng et al., 2012). Numerous studies have demonstrated that VGCC levels correlate highly with P_r (Akbergenova *et al.*, 2018; Gratz *et al.*, 2019; Holderith *et al.*, 2012; Nakamura *et al.*, 2015; Sheng *et al.*, 2012). Paradoxically, this is not always the case. For example, a recent study investigated two cerebellar synaptic subtypes, one high-P_r formed by stellate cells and one low-P_r formed by granule cells, and found higher VGCC levels at low-P_r granule synapses (Rebola *et al.*, 2019). This finding highlights the importance of synaptic context in understanding the role of VGCC levels in determining P_r at distinct synapses. Since VGCCs in closer proximity to release sites are expected to have a greater impact on vesicular release probability than

those positioned farther away, the spatial coupling of VGCCs and SVs at AZs is a critical determinant of P_r (Chen *et al.*, 2015; Eggermann et al., 2011; Fedchyshyn and Wang, 2005; Nakamura *et al.*, 2015; Rebola *et al.*, 2019). Indeed, at high-P_r stellate synapses, a 'perimeter release' AZ organization places VGCCs ~40nm closer to SVs than at low-P_r granular synapses (Rebola *et al.*, 2019). How these distinct topographies are set remains unknown.

To better understand the context-dependent contributions of VGCCs to heterogeneous neurotransmitter release properties, we sought a system where we could investigate the relationship between VGCCs and P_r at two closely related neurons that form synapses with distinct release probabilities. *Drosophila* muscles are innervated by two glutamatergic motor neurons, one tonic and one phasic, that form type Ib and type Is synapses, respectively. Type Ib synapses have relatively low P_r and facilitate, whereas type Is synapses have higher P_r and depress in response to high-frequency stimulation (Aponte-Santiago et al., 2020; Lnenicka and Keshishian, 2000). In this study, we investigated how VGCC number, organization, and subunit composition contribute to synaptic heterogeneity at low-P_r type Ib and high-P_r type Is inputs. We find that individual synapses formed by both low- and high-P_r inputs exhibit heterogeneous release properties that can be predicted by VGCC levels alone. However, VGCC levels do not correspond to differences in P_r between the two inputs due to underlying molecular and organizational differences that alter the relationship between VGCC levels and P_r at AZs of low- vs. high-P_r inputs. These findings reveal intersecting levels of molecular and spatial diversity that combine to generate extensive synaptic heterogeneity.

RESULTS

VGCC levels predict P_r within, but not between, synaptic subtypes

To investigate the relationship between VGCC levels and neurotransmitter release properties at functionally distinct synapses, we took advantage of the two motor neuron subtypes with low and high release probabilities that innervate most *Drosophila* muscles (Aponte-Santiago and Littleton, 2020; Kurdyak et al., 1994). These glutamatergic neuromuscular junctions (NMJs) contain hundreds of

individual synapses that are accessible to single AZ functional imaging using genetically encoded Ca^{2+} indicators.

In *Drosophila*, Cacophony (Cac) is the sole Ca_v2 pore-forming subunit and is the VGCC responsible for triggering synaptic transmission (Kawasaki et al., 2000; Macleod et al., 2006; Peng and Wu, 2007; Smith et al., 1996). To simultaneously monitor neurotransmitter release and VGCC levels, we swapped the N-terminal sfGFP tag in our well-characterized *cac*$^{sfGFP\text{-}N}$ line for a Td-Tomato tag (*cac*$^{Td\text{-}Tomato\text{-}N}$). We have previously incorporated a number of protein tags at this site without disrupting function and confirm below that a larger tandem tag does not impair synaptic function (See Figs 1A-F; (Ghelani et al., 2023; Gratz *et al.*, 2019)). We then expressed postsynaptically targeted GCaMP6f (SynapGCaMP6f; (Newman et al., 2017)), which reports Ca^{2+} influx through glutamate receptors in response to neurotransmitter release in *Cac*$^{Td\text{-}Tomato\text{-}N}$ animals. We and others have previously shown that Cac levels are highly predictive of P_r at individual type Ib AZs (Akbergenova *et al.*, 2018; Gratz *et al.*, 2019). To determine if VGCC levels are similarly predictive at high-P_r type Is AZs, we measured $Cac^{Td\text{-}Tomato\text{-}N}$ fluorescence intensity and monitored neurotransmitter release in response to 0.2-Hz stimulus at individual synapses. To enable direct comparisons between the two synaptic subtypes, we simultaneously imaged type Ib and type Is synapses at NMJ 6/7 (Fig. 1A). We quantified the number of times a vesicle was released over 120 stimuli to determine single-synapse P_r, and found that, as expected, type Is synapses exhibited significant heterogeneity and higher average P_r than type Ib synapses (Fig. 1B, C; (Newman *et al.*, 2022)). Consistent with their higher P_r, type Is connections contain relatively fewer low-P_r AZs (Figs. 1D, (Jetti et al., 2023)). We next investigated the correlation between P_r and VGCC levels and found that at type Is inputs, single-AZ Cac intensity positively correlates with P_r (Fig. 1E; REFS). We also observe a strong positive correlation between VGCC levels and P_r at type Ib inputs (Fig. 1F), consistent with our and others' prior findings (Akbergenova *et al.*, 2018; Gratz *et al.*, 2019; Newman *et al.*, 2022).

A simple prediction of the observation that VGCC levels correlate highly with P_r at individual AZs of both low- and high-P_r inputs is that, when comparing between them, Cac levels will be higher at type Is inputs than type Ib. We analyzed $Cac^{sfGFP\text{-}N}$ levels at individual AZs of type Ib and Is motor neurons and found that average Cac levels are the same at type Ib and Is AZs (Fig. 1G, H). Cac levels are also similarly distributed across active zones of the two inputs (Fig 1I). Together, these findings indicate that the relationship between VGCC levels and P_r differs between the two inputs. Consistently, when we compare the relationship between Cac levels and P_r at the type Ib and Is inputs from our correlative functional imaging data, we find that the slopes of the best-fit lines are significantly different (Fig. 1J). Across type Is active zones, a similar range of VGCC levels supports a broader range of release probabilities. Thus, VGCCs can predict P_r within synaptic subtypes, but not between active zones of different synaptic subtypes, providing a framework for understanding seemingly contradictory findings on the role of VGCCs in determining P_r.

VGCC clusters are more compact at AZs of high-P_r type Is inputs

To understand how spatial differences might alter the relationship between VGCC levels and P_r at low-P_r type Ib and high-P_r type Is AZs, we turned to 3D dSTORM single-molecule localization microscopy (SMLM). An individual VGCC complex is estimated to be ~10 nm in diameter with the most common immunolabeling techniques adding significantly to their size and creating a linkage error of ~20 nm between the target molecule and fluorescent reporter (Früh et al., 2021; Liu et al., 2022; Thomas, 2000). For following VGCC dynamics using single-particle tracking via photoactivation localization microscopy (sptPALM), we recently incorporated mEOS4b (Paez-Segala et al., 2015) at the N-terminus of Cac, achieving a linkage error of less of than 5 nm (Ghelani *et al.*, 2023). To gain more flexibility in labeling Cac without adding to the linkage error, we swapped the mEOS tag for a similarly sized HaloTag ($cac^{HaloTag\text{-}N}$). As expected, these flies are fully viable and $Cac^{HaloTag\text{-}N}$ exhibits normal localization to AZs, where Brp is arranged in a ring that surrounds a puncta of VGCCs in superresolution optical reassignment images (Fig. 2A-C; (Ghelani *et al.*, 2023; Gratz *et al.*, 2019)). HaloTag, which covalently binds synthetic ligands, is 3.3 nm in diameter (Los et al., 2008; Yazaki et al.,

2019), yielding a linkage error well under 5 nm.

$Cac^{HaloTag-N}$ larvae were stained with JaneliaFluor646 HaloTag ligand (Grimm et al., 2015) and horseradish peroxidase (HRP) to distinguish between type Ib and Is branches and enable simultaneous imaging of the two synaptic subtypes innervating NMJ 6/7. We then used density-based spatial clustering of applications with noise (DBSCAN) analysis to identify Cac clusters at type Ib and Is AZs (Fig. 2D,E; (Ehmann et al., 2014)). We find that the average size of $Cac^{HaloTag-N}$ clusters is similar at low- and high-P_r AZs (Fig. 2F), with mean diameters of approximately 102 nm and 105 nm, respectively. This is similar to the $Cac^{mEOS4b-N}$ type Ib cluster size observed by sptPALM imaging (Ghelani *et al.*, 2023). In agreement with our confocal level data, the number of localizations per cluster was similar at low- and high-P_r AZs (Fig. 2G). We then calculated the average Cac density per AZ, and found that VGCCs are significantly more densely organized at high-P_r type Is AZs than low-P_r type Ib AZs (Fig. 2H, I). Greater AZ density at type Is AZs is consistent with recent SMLM studies using antibodies to label Cac or Brp (Mrestani et al., 2021; Newman *et al.*, 2022) and a recent electrophysiological analysis of VGCC-SV coupling that revealed significantly tighter coupling at type Is synapses (He et al., 2022). Together, these findings suggest that more compact organization of VGCCs increases their proximity to SVs and contributes to the steeper relationship between VGCC levels and P_r at high-P_r type Is AZs.

Differences in Bruchpilot levels and function at low- and high-P_r inputs

To understand how these nanoscale differences in VGCC organization might be established, we investigated the AZ scaffolding protein Bruchpilot (Brp). Brp/CAST/ELKs family proteins function as central organizers of both VGCCs and SV release sites at developing synapses (Dai et al., 2006; Dong et al., 2018; Hallermann et al., 2010; Held et al., 2016; Kittel et al., 2006; Liu et al., 2014; McDonald et al., 2020; Radulovic et al., 2020).

We simultaneously imaged type Ib and Is inputs and found lower Brp levels at type Is AZs (Fig. 3A, B). Since Cac levels are similar at the two synaptic subtypes, lower Brp levels result in a significantly higher Cac:Brp ratio at type Is synapses, which we hypothesize promotes compact organization of VGCCs (Fig. 3C). In contrast, we and others have previously shown that Brp levels positively correlate with P_r among AZs of low-P_r type Is inputs (Gratz *et al.*, 2019; Muhammad et al., 2015; Newman *et al.*, 2017; Peled et al., 2014; Reddy-Alla *et al.*, 2017). Consistently, Brp and Cac levels strongly correlate at type Ib AZs (Gratz *et al.*, 2019) and we observe a similarly strong correlation across individual type Is AZs (Fig. 3D). Thus, like VGCCs, Brp levels contribute in distinct ways to synaptic heterogeneity within vs. between low- and high-P_r synaptic subtypes depending on input-specific AZ organization.

We next investigated the requirement for Brp in promoting VGCC accumulation at low- and high-P_r inputs by analyzing $Cac^{sfGFP\text{-}N}$ levels in *brp* null mutants ($brp^{-/-}$; Fig. 3E, F). $Cac^{sfGFP\text{-}N}$ levels are diminished at both type Ib and Is AZs, demonstrating a conserved role for Brp in promoting Cac accumulation at both synaptic subtypes (Fig. 3G). Strikingly, the relative decrease in Cac levels at type Ib AZs is significantly greater than at type Is AZs, indicating a greater requirement for Brp in regulating VGCC levels at low-P_r type Ib synapses (Fig. 3H). This suggests that an additional factor or factors function with or upstream of Brp to establish differences between low and high-P_r AZs.

Brp differentially regulates VGCC dynamics at low- and high-P_r synapses during presynaptic homeostatic potentiation

In response to acute or chronic inhibition of glutamate receptors at NMJs, *Drosophila* motor neurons homeostatically increase neurotransmitter release to maintain synaptic communication (Davis and Muller, 2015; Frank, 2014; James et al., 2019). Pharmacological inhibition of glutamate receptors with the wasp toxin Philanthotoxin-433 (PhTx) induces acute presynaptic homeostatic potentiation of release (PHP) within minutes (Frank et al., 2006). We and others have demonstrated that acute PHP involves rapid changes in VGCCs and other AZ protein levels at AZs of type Ib inputs (Bohme et al., 2019; Gratz *et al.*, 2019; Weyhersmuller et al., 2011). Recent studies have revealed significant

differences in the induction of PHP at low- and high-P_r synaptic inputs under different conditions (Genc and Davis, 2019; Newman *et al.*, 2017; Sauvola *et al.*, 2021). PhTx induces acute PHP at both type Ib and Is synapses (Genc and Davis, 2019), but the molecular changes underlying PHP at high-P_r type Is AZs remain unknown. To compare the dynamic modulation of VGCCs at low- and high-P_r AZs, we treated *cac*$^{sfGFP\text{-}N}$ larvae with non-saturating concentrations of PhTx for 10 min, then quantified Cac and Brp levels at type Ib and Is AZs (Fig. 4A, B). We observe a significant PhTx-induced increase in Brp and Cac$^{sfGFP\text{-}N}$ levels at type Is AZs similar to type Ib (Fig. 4C, D; (Gratz *et al.*, 2019)). Thus, despite their distinct baseline transmission and organizational properties, PhTx-induced potentiation of neurotransmitter release involves rapid accumulation of VGCCs at both low- and high-P_r AZs.

At low-P_r type Ib AZs, Brp is a critical regulator of PHP-induced accumulation of proteins associated with SV priming and release, specifically Unc13A and Syntaxin-1A (Bohme *et al.*, 2019). At type Ib AZs, PhTx also induces a Brp-dependent increase in Cac density and decrease in channel mobility (Ghelani *et al.*, 2023). Notably, Brp itself is more densely organized during PHP (Ghelani *et al.*, 2023) and at high-P_r type Is AZs (Mrestani *et al.*, 2021). Since baseline accumulation of VGCCs depends less on Brp at high-P_r type Is AZs, we investigated the role of Brp in promoting dynamic increases in VGCC levels at type Ib and Is AZs by treating *cac*$^{sfGFP\text{-}N}$*; brp*$^{-/-}$ larvae with PhTx followed by quantification of Cac$^{sfGFP\text{-}N}$ levels (Fig. 4E, F). We find that PhTx failed to induce accumulation of Cac at either type Ib or Is AZs in *brp*$^{-/-}$ mutants, demonstrating a shared requirement for Brp in regulating VGCC dynamics at low- and high- P_r AZs (Fig 4G). Notably, in contrast to no change at type Ib AZs, Cac$^{sfGFP\text{-}N}$ levels are significantly decreased at type Is AZs (Fig 4G), revealing subtype-specific roles for Brp during the dynamic reorganization of VGCCs at low- and high-P_r AZs. Consistently, Ghelani et al. (2023) found that whereas PhTx induces a decrease in the Cac mobility at wild-type type Ib AZs, in *brp*$^{-/-}$ mutants Cac mobility increases (Ghelani *et al.*, 2023). Together, these findings suggest potentiating synapses must coordinate the accumulation of new VGCCs with the stabilization of existing channels, and that meeting this challenge is more dependent upon Brp at high-P_r AZs.

Endogenous tagging of VGCC auxiliary subunits reveals distinct synaptic expression patterns

In addition to spatial organization, functional differences in the VGCCs localized at low- and high-P_r AZs may contribute to differences in the relationship between channel levels and P_r. Consistent with this possibility, Ca^{2+} influx is reported to be ~2x higher at type Is AZs and neurotransmitter release saturates at lower external Ca^{2+} concentrations than type Ib AZs (He *et al.*, 2022; Lu et al., 2016). In addition to the pore-forming α subunits, VGCCs comprise auxiliary α2δ and β subunits that regulate forward channel trafficking, membrane insertion, and function (Fig. 5A; (Campiglio and Flucher, 2015; Dolphin and Lee, 2020; Weiss and Zamponi, 2017)). β subunits interact with pore-forming α subunits intracellularly, whereas GPI-anchored α2δ subunits are largely extracellular. In addition to their interaction with α subunits, α2δs have been shown to interact with a growing number of extracellular proteins to promote synaptogenesis (Bauer et al., 2010; Dolphin, 2018). The *Drosophila* genome encodes one synaptic Ca_v2 α subunit (Cac), one β subunit, and three α2δ subunits (Littleton and Ganetzky, 2000). Auxiliary subunits are both spatially and temporally regulated, and broadly able to interact with α subunits. Thus, the subunit composition of channel complexes is a potential source of significant diversity in both the spatial and functional regulation of VGCCs.

ca-β encodes the sole *Drosophila* β subunit and has been shown to enhance Ca^{2+} transients in sensory neurons (Kanamori et al., 2013). *Drosophila* α2δ-3, also known as Straightjacket (Stj), has well-characterized roles at the NMJ in promoting Ca^{2+} channel clustering, homeostatic plasticity, and, independently of Cac, synapse formation and organization (Dickman et al., 2008; Hoover et al., 2019; Kurshan et al., 2009; Ly et al., 2008; Wang et al., 2016). The remaining two α2δ subunits don't map to a specific mammalian counterpart. CG4587/Stolid was recently shown to promote dendritic Cac expression in motor neurons, whereas Ma2d is known to function in muscle where it is broadly expressed (Heinrich and Ryglewski, 2020; Reuveny et al., 2018). The synaptic localization of endogenous auxiliary subunits with VGCCs remains unknown in *Drosophila*. To explore potential differences in VGCC subunit composition at type Ib and Is synapses, we used CRISPR gene editing to incorporate endogenous V5 tags at the N-termini of Stj and Stolid and C-terminus of Ca-β, and

confirmed that the incorporation of the peptide tag did not impair neurotransmission (Fig. 5B-E; (Bruckner et al., 2017; Gratz et al., 2014). We investigated the expression of each endogenously tagged subunit in the larval ventral ganglion and found that all subunits are expressed in the synaptic neuropil in a pattern similar to the α subunit Cac (Fig. 5F-H; (Gratz *et al.*, 2019)). Similar to Cac, Ca-β^{V5-C} is highly enriched in the mushroom bodies of the larval brain. We next investigated expression at the larval NMJ where Cac localizes in a single puncta at each AZ and found that only Ca-β^{V5-C} and Stj^{V5-N} are present (Fig. 5F-H). This aligns with a recent study indicating that Stolid does not play a role in regulating Ca^{2+} transients at the larval NMJ (Heinrich and Ryglewski, 2020). We also observe Ca-β^{V5-C} expression in muscle as expected for the sole β subunit (Fig. 5F and see Fig. 6C).

Stj/α2δ-3 levels are lower at AZs of high-P_r type Is inputs

To investigate $Ca\beta^{V5-C}$ and Stj^{V5-N} localization at type Ib and Is AZs, we used superresolution optical reassignment microscopy. Both subunits localize to AZs labeled with Cac or the CAST/ELKS AZ cytomatrix protein Brp (Fig 6A, B). We observe Brp rings surrounding puncta of VGCCs, including the Ca-β^{V5-C} and, based on its colocalization with Cac, Stj^{V5-N} subunits (Fig. 6A, B; (Fouquet et al., 2009b; Kittel *et al.*, 2006)). Their tight colocalization at AZs suggest that the three subunits associate as a complex and predict that Ca-β^{V5-C} and Stj^{V5-N} levels, like Cac, will be similar at the two synapses. To compare subunit levels at low- and high-P_r AZs, we simultaneously imaged type Ib and Is inputs using confocal microscopy and measured fluorescence intensity (Fig. 6C, D). As predicted, we found that Ca-β^{V5-C} levels are similar at type Ib and Is AZs (Fig. 6E). In contrast, Stj^{V5-N} fluorescence levels are significantly lower at higher-P_r type Is AZs (Fig. 6F). Thus, while Cac and Ca-β are present in similar ratios at both synaptic subtypes, surprisingly, the same is not true of Stj/α2δ-3 with high-P_r type Is AZs exhibiting a greater Cac:Stj ratio. This unexpected finding is consistent with studies of mammalian subunits indicating that in contrast to β subunits, α2δ interactions with α subunits may be transient, leading to a pool of VGCCs lacking α2δ (Muller et al., 2010; Voigt et al., 2016). Our results suggest this pool is present *in vivo* and larger at high-P_r type-Is inputs.

To further investigate the contribution of Stj to synaptic heterogeneity, we analyzed the relationship between Cac and Stj levels at individual AZs of type Is inputs. $Stj^{V5\text{-}N}$ and $Cac^{sfGFP\text{-}N}$ levels are highly positively correlated at type Is AZs (Fig. 6G). We observe the same relationship between $Stj^{V5\text{-}N}$ and $Cac^{sfGFP\text{-}N}$ levels at type Ib AZs (Fig. 6H). Because P_r is highly positively correlated with Cac levels within synaptic subtypes, this indicates that Stj levels are also positively correlated with P_r within, but not between, synaptic subtypes. Together, these findings reveal context-specific contributions of VGCC levels and composition to synaptic heterogeneity.

DISCUSSION

Complex nervous system function depends on communication at synapses with heterogeneous properties. We have investigated the contributions of VGCC levels, organization, and subunit composition to synaptic heterogeneity at two closely related excitatory neurons that form synapses with distinct neurotransmitter release properties. This approach revealed that while VGCC levels alone are predictive of the strength of individual synapses within neuronal subtypes, underlying differences in spatial and molecular organization alter the relationship between channel levels and release probability at synapses formed by distinct neuronal subtypes. This provides a framework for understanding how multiple levels of molecular and organizational diversity intersect to generate extensive synaptic heterogeneity.

Investigations at diverse synapses using approaches ranging from cell-attached patch recordings to freeze-fracture immuno-electron microscopy to correlative functional imaging have revealed a strong positive correlation between VGCC number and P_r (Akbergenova *et al.*, 2018; Gratz *et al.*, 2019; Holderith *et al.*, 2012; Nakamura *et al.*, 2015; Sheng *et al.*, 2012). While this conclusion corresponds neatly with the dependence of neurotransmitter release on Ca^{2+} influx, counterintuitively, there is a disconnect between VGCC levels and P_r at some synapses. Although VGCC number positively correlates with P_r at the immature calyx of Held, the mature calyx contains fewer VGCCs despite higher P_r (Fedchyshyn and Wang, 2005; Sheng *et al.*, 2012; Wang and Augustine, 2014). Similarly, in the

cerebellum, inhibitory stellate neurons form high-P_r synapses with lower VGCC levels than low-P_r synapses formed by excitatory granular neurons (Rebola *et al.*, 2019). Adding to these paradoxical examples, VGCC levels positively correlate with P_r among the heterogeneous synapses formed by either low-P_r type Ib or high-P_r type Is motor neurons, but overall VGCC levels are are similar at type Ib and Is inputs despite a 2-3-fold difference in P_r (Fig. 1, 2; (Lu *et al.*, 2016; Newman *et al.*, 2017). Accordingly, correlative functional imaging confirms that the same number of channels can support greater release at these high-P_r AZs (Fig. 1). This difference is likely due, at least in part, to distinct spatial organization at type Is AZs. Cac clusters are denser at high-P_r AZs (Fig. 2). Brp, which organizes both VGCCs and SVs, is also more densely organized at type Is synapses (Mrestani *et al.*, 2021), consistent with an overall more compact organization of high-P_r AZs. A straightforward prediction is that a more compact AZ organization will decrease the distance between VGCCs and SVs. Indeed, a recent electrophysiological study using new tools for genetically isolating type Ib and Is inputs demonstrated that neurotransmitter release at denser type Is synapses is less impacted by the slow Ca^{2+} chelator EGTA than type Ib synapses, indicating tighter VGCC-SV coupling (He *et al.*, 2022). More densely organized VGCCs at the mature vs. developing calyx of Held also exhibit greater coupling with SVs (Chen *et al.*, 2015; Fedchyshyn and Wang, 2005; Fekete *et al.*, 2019; Nakamura *et al.*, 2015; Sheng *et al.*, 2012). Similarly, high-P_r stellate synapses have greater functional coupling attributable to their more compact topology (Rebola *et al.*, 2019). Together, these findings suggest that more compact AZs may be a general organizing principle of high-P_r synapses. We propose that underlying organizational differences between low- and high-P_r synaptic subtypes combine with molecular diversity within each subtype to generate still greater synaptic heterogeneity. This explains our observation that VGCC levels, as well as Brp and Stj levels, predict P_r within, but not between, synaptic subtypes, as well as the seemingly paradoxical findings that VGCC levels do not always correlate with P_r.

Brp/CAST/ELKS AZ cytomatrix proteins are central regulators of synapse organization across species (Dai *et al.*, 2006; Dong *et al.*, 2018; Hallermann *et al.*, 2010; Held *et al.*, 2016; Kittel *et al.*, 2006; Liu *et al.*, 2014; McDonald *et al.*, 2020; Radulovic *et al.*, 2020). Brp interacts with a large number of AZ

proteins to promote Cac clustering at AZs, organize SVs, and recruit Unc13A, which defines SV release sites (Bohme et al., 2016; Fulterer et al., 2018; Ghelani *et al.*, 2023; Liu et al., 2011). Consistently, type Is AZs, which in addition to increased Brp density also have lower Brp levels (Fig. 3) and fewer release sites (He *et al.*, 2022; Jetti *et al.*, 2023; Mrestani *et al.*, 2021). Given Brp's myriad interactions, it is not difficult to envision its compaction bringing VGCCs and SVs in closer proximity and leading to higher P_r independent of the overall number of release sites and Cac levels. Consistent with this model, Brp density increases during PHP, extending the positive relationship between AZ density and P_r to dynamic changes in release properties (Mrestani *et al.*, 2021). This denser Brp scaffold also promotes PhTx-induced increases in Cac levels and density along with the addition and reorganization of release sites (Fig. 4; (Bohme *et al.*, 2019; Dannhauser et al., 2022; Ghelani *et al.*, 2023). While Brp clearly plays a central role in AZ organization and reorganization, we find that type Ib and Is synapses have distinct requirements for Brp during synapse formation and homeostatic potentiation (Fig. 3, 4). Synapse-specific roles for Brp are supported by a recent functional imaging study in *Drosophila* (Jetti *et al.*, 2023) and studies of ELKS at mammalian inhibitory and excitatory synapses (Held *et al.*, 2016), and suggest that Brp acts in parallel with or downstream of other factors that establish neuron-specific differences. A recent single-cell transcriptomic study of type Ib and Is motor neurons provides an unbiased starting point for identifying candidate regulators of organizational differences at low- and high-P_r AZs (Jetti *et al.*, 2023). A number of cytoskeletal and motor-related proteins, regulators of proteostasis, and post-translational modifying enzymes/pathway components – all of which could potentially contribute to establishing the observed molecular and/or spatial differences – are differentially expressed in either type Ib or Is motor neurons

The VGCC complex itself provides an additional potential mechanism for diversifying synapses. Both β and α2δ subunits can influence the membrane localization and function of VGCCs. In addition to the ability to mix and match subunits, many of the genes encoding VGCC subunits across species are extensively alternatively spliced to generate functional diversity (Lipscombe et al., 2013; Lipscombe and Lopez Soto, 2019) – an area of great interest for further investigation. Because both β and α2δ subunits

are generally considered positive regulators of channel trafficking and function, we were surprised to find that Stj/α2δ-3 levels are lower at high-P_r AZs (Figs. 5, 6). Since AZ levels of α subunit Cac are similar at the two synaptic subtypes, lower levels of Stj at type Is synapses indicates a difference in α:α2δ-3 stoichiometry. The stoichiometry of α:α2δ appears to vary. While some studies observe a tight association between the two subunits, a single-molecule tracking study of mammalian VGCCs found that α2δ subunits have a relatively low affinity for α subunits, resulting in a population of α subunits not associated with an α2δ subunit (Cassidy et al., 2014; Voigt *et al.*, 2016). Consistently, whereas α and β subunits were isolated at near equimolar ratios following affinity purification of Ca_v2 channels, molar levels of α2δ were a surprising 90% lower (Muller *et al.*, 2010). Our findings suggest there is a pool of VGCCs lacking an α2δ subunit at endogenous synapses, and further suggest that this pool is greater at high-P_r type Is AZs. Stj is both required (Dickman *et al.*, 2008; Kurshan *et al.*, 2009; Ly *et al.*, 2008) and rate limiting (Cunningham et al., 2022) for Cac accumulation at AZs. Stj does not appear to function in the stabilization of channels at the AZ membrane, but rather at an upstream step in the progression from ER to plasma membrane (Cunningham *et al.*, 2022). An upstream role may explain how Cac levels are similar at type Is AZs despite lower Stj levels. Tools for following Stj dynamics in developing neurons will help clarify its precise role in Cac delivery. How might a higher α:α2δ-3 ratio result in higher P_r? A number of recent studies raise intriguing possibilities. While the correspondence of *Drosophila* α2δ subunits to specific mammalian counterparts is somewhat murky, Stj appears to be most closely related to α2δ-3. Strikingly, α2δ-3 inhibits activity at excitatory synapses of mature, but not immature, rat hippocampal cultures (Bikbaev et al., 2020), raising the possibility that Stj's role may shift during synapse maturation. Further, binding of the cell adhesion molecule Neurexin-1α specifically inhibits Ca^{2+} currents in $Ca_v2.2$ channels containing α2δ-3 (Tong et al., 2017), which, if similar at the *Drosophila* NMJ, would result in greater inhibition of channel function at type Ib AZs and contribute to the observed difference in Ca^{2+} influx. Elucidating the many intersecting mechanisms underlying synaptic heterogeneity and how these differences are maintained or modulated during different forms of plasticity is a challenging and important goal for the field going forward.

MATERIALS AND METHODS

Drosophila genetics and gene editing

The following fly lines used in this study are available at the Bloomington Drosophila Stock Center (BDSC): w^{1118} (RRID:BDSC_5905), *vasa-Cas9* (RRID:BDSC_51324), piggyBac transposase (RRID:BDSC_8283), and Df(2R)brp$^{6.1}$ (Gratz *et al.*, 2014; Horn et al., 2003). *brp* alleles were generously provided by Stephan Sigrist (Freie Universität Berlin; (Fouquet et al., 2009a; Kittel *et al.*, 2006). *brp* loss-of-function experiments were performed in *brp*^{69}/Df(2R)brp6.1. *Drosophila melanogaster* stocks were raised on molasses food (Lab Express, Type R) in a 25°C incubator with controlled humidity and 12h light/dark cycle. Endogenously tagged *cac*, *ca-β*, *stolid*, and *straightjacket* (*stj*) alleles were generated using our piggyBac-based CRISPR approach as previously detailed (flyCRISPR.molbio.wisc.edu; Bruckner et al., 2017, Gratz et al., 2019). Endogenous tags were incorporated at the N-terminus of Cac, which has been shown to support a variety of tags, to make Cac$^{\text{Td-Tomato-N}}$ and Cac$^{\text{HaloTag-N}}$ (Gratz et al., 2019, Cunningham, Ghelani et al., 2023). V5 tags were incorporated at the N-terminus of Stj and Stolid after their respective signal peptide sequences and in the last common exon of Ca-β near the C terminus of shorter isoforms. All CRISPR-generated lines are fully viable in homozygous males and females and were molecularly confirmed by Sanger sequencing.

Immunostaining

All antibodies used, associated fixation methods, and incubation times can be found in Table S2. Male wandering third-instar larvae were dissected in ice-cold saline and fixed either for 6 minutes at room temperature with Bouin's fixative, 5 minutes on ice with 100% methanol, or 30 minutes at room temperature (RT) in 4% PFA. Dissections were permeabilized with PTX (PBS with 0.1% Triton-X 100) and blocked for 1 hour at RT using 5% goat serum and 1% bovine serum albumin. Stained larvae were mounted in Vectashield (Vector Laboratories, #H-1000) under Fisherbrand coverglass (Fisher Scientific, #12541B) for confocal microscopy, with Prolong glass mounting medium (ThermoFisher Scientific, #P36980) under Zeiss High Performance Coverglass (Zeiss, #474030-9000-000) for

superresolution optical reassignment microscopy, or buffer (see STORM imaging and analysis section) under Zeiss coverglass with edges sealed using vacuum grease for STORM microscopy.

Ca^{2+} imaging and analysis

Functional imaging was performed on a Nikon A1R resonant scanning confocal mounted on a FN1 microscope using a Nikon Apo LWD 25x 1.1 NA objective and a Mad City Labs piezo drive nosepiece. Dissections and data collection were performed as previously described in Gratz et al., 2019. Briefly, *$Cac^{Td\text{-}Tomato\text{-}N}$*; *Mhc*-GCaMP6f male 3rd instar larvae were dissected in HL3 containing 0.2mM Ca^{2+} and 25mM Mg^{2+} with motor axons severed and the larval brain removed. Larval filets were placed in HL3 containing 1.5mM Ca^{2+} and 25mM Mg^{2+} for recording. Nerves were suctioned into 1.5mm pipettes and stimulus amplitude was adjusted to recruit both type Ib and type Is input. Motor terminals from segments A2-4 at NMJ 6/7 were imaged for $Cac^{Td\text{-}Tomato\text{-}N}$ levels first using a galvanometer scanner, then a resonant scanner to collect GCaMP6f events in a single focal plane continuously for 120 stimulations at a 0.2 Hz stimulation frequency.

Z-stacks and movies were loaded into Nikon Elements Software (NIS) where movies were motion corrected, background subtracted, and denoised. Change in fluorescence (ΔF) movies were then created by subtracting the average of the previous 10 frames from each frame. A substack of only stimulation frames was further processed using a gaussian filter followed by BrightSpots detection to identify the location of each postsynaptic event using the Nikon GA3 module. $Cac^{Td\text{-}Tomato\text{-}N}$ fluorescence intensity levels and coordinate locations were measured for 531 AZs for type Ib and 365 AZs for type Is terminals across 6 animals. X-Y coordinate positions of fluorescent signals from GCaMP6f postsynaptic events were aligned to $Cac^{Td\text{-}Tomato\text{-}N}$ puncta locations and each post synaptic event assigned to a Cac puncta using nearest neighbor analysis. Postsynaptic events that did not map within 960 nm of a $Cac^{Td\text{-}Tomato\text{-}N}$ punctum were discarded from the analysis. Pearson's correlation was used to determine the correlation between P_r and Cac levels normalized to average to account for variability between imaging sessions. Cac intensity-P_r heat maps were generated using Python matplotlib and seaborn plotting

packages.

STORM imaging and analysis

STORM imaging was performed on a Nikon Eclipse Ti2 3D NSTORM with an Andor iXon Ultra camera, Nikon LUN-F 405/488/640 nm lasers, and a Nikon 100x 1.49 NA objective. STORM buffer (10mM MEA (pH 8.0), 3 U/mL pyranose oxidase, and 90 U/mL catalase, 10% (w/v) glucose, 10 mM sodium chloride, and 50 mM Tris hydrochloride) was made fresh each imaging day and pH adjusted to between 7.0-8.0 using acetic acid. $Cac^{HaloTag\text{-}N}$ NMJs were labeled as detailed in Table S2 and immediately imaged for HRP in 488 channel to identify type Ib and type Is terminals. $Cac^{HaloTag\text{-}N}$ was then imaged using the 640 nm laser line at 33 Hz for 5000 frames. 405 nm laser power was gradually increased over the course of imaging to compensate for run-down of blinking rates. A back aperture camera was used to ensure beam focus and position for each imaging session to ensure high signal to noise. Data were binned with a CCD minimum threshold of 100 and drift correction was applied using the NIS Software STORM package. ROIs of single boutons were drawn in NIS using HRP in the 488 nm channel followed by a DBSCAN analysis with criteria of 10 molecules within 50 nm to determine clusters. Positional coordinates of localizations within clusters from DBSCAN were exported from NIS and run through a Python script published with this manuscript. Using the implementation developed in Mrestani et al., 2021 as a starting point, we wrote custom code to use the alpha shapes component of the CGAL package (https://www.cgal.org), via a python wrapper (https://anaconda.org/conda-forge/cgal), to measure the area of Ca^{2+} channel clusters, the number of localizations, and calculate cluster density. To achieve an average lateral localization accuracy of ~30 nm, all localizations with >50 nm localization accuracy were removed prior to analysis. Using this custom code, $Cac^{HaloTag\text{-}N}$ area was analyzed using an alpha value of 0.015, which controls the complexity of cluster boundaries (not restricted to be convex).

Confocal imaging and analysis

For quantitative AZ analysis, larvae stained in the same dish were imaged on a Nikon Eclipse Ni A1R+

confocal microscope using an Apo TIRF 60x 1.49 NA oil-immersion objective for larval NMJs. NMJs containing both type Is and type Ib branches from muscles 6/7 in segments A2-4 were collected. ROIs were drawn using HRP staining to differentiate between type Ib and type Is branches. To analyze individual AZs, Nikon Elements Software was used to process images using Gaussian and rolling ball filters and analyze fluorescence intensity levels for individual puncta. When experimental design allowed, Brp fluorescence signal was used to create a binary mask to aid in the identification of AZ ROIs for analysis. Otherwise, binary masks were created based on the fluorescence signal of the channel analyzed. Confocal fluorescence intensity level data are reported as the sum fluorescence intensity per AZ averaged over individual NMJs. For Fig. 5, larvae were stained separately and imaged using a Nikon Plan-Apo 20x 0.75 NA objective (ventral ganglia) or Apo TIRF 60x 1.49 NA oil-immersion objective (NMJs).

Superresolution optical reassignment images were obtained on a Nikon CSU-W1 SoRa (Spinning Disk Super Resolution by Optical Pixel Reassignment) with a Photometrics Prime BSI sCMOS camera and a 60x 1.49 NA oil-immersion objective. Images were acquired using Nikon NIS and deconvolved using Richardson-Lucy deconvolution with 15-20 iterations.

Electrophysiology

Current-clamp recordings were performed as previously described (Bruckner, 2017). Male third-instar larvae were dissected in HL3 (70 mM NaCl, 5 mM KCl, 15 mM MgCl2, 10 mM NaHCO3, 115 mM sucrose, 5 mM trehalose, 5 mM HEPES, pH 7.2) with 0.25 mM Ca^{2+}. Recordings were performed in HL3 at the external Ca^{2+} concentration indicated. Sharp borosilicate electrodes filled with 3 M KCl were used to record from muscle 6 of abdominal segments A3 and A4. Recordings were conducted on a Nikon FN1 microscope using a 40x 0.80 NA water-dipping objective and acquired using an Axoclamp 900A amplifier, Digidata 1550B acquisition system, and pClamp 11.0.3 software (Molecular Devices).

For each cell with an initial resting potential between −60 and −80 mV and input resistance ≥5 MΩ,

mean miniature excitatory junctional potentials (mEJPs) were collected for 1 minute in the absence of stimulation and analyzed using Mini Analysis (Synaptosoft). EJPs were generated by applying a stimulus to severed segmental nerves at a frequency of 0.2 Hz using an isolated pulse stimulator 2100 (A-M Systems). Stimulus amplitude was adjusted to consistently elicit compound responses from both type Ib and Is motor neurons. At least 25 consecutive EJPs were recorded for each cell and analyzed in pClamp to obtain mean amplitude. Quantal content was calculated for each recording as mean EJP amplitude divided by mean mEJP amplitude.

Acute homeostatic challenge

Acute PHP was induced by incubating semi-intact preparations in 20 µM Philanthotoxin-433 (PhTx; Santa Cruz, sc-255421, Lot B1417) diluted in HL3 containing 0.4 mM Ca^{2+} for 10 min at room temperature (Frank et al., 2006). Control preparations were given a mock treatment. Following control and experimental treatment, dissections were completed, fixed in 4% PFA for 30 minutes, and stained for $Cac^{sfGFP\text{-}N}$ and Brp in the same dish. Analyses of fluorescent intensity levels were performed as previously described in the *Confocal imaging and analysis section.*

Experimental Design and statistical analysis

Statistical analyses were conducted in GraphPad Prism 9. Normality was determined by the D'Agostino–Pearson omnibus test. Comparisons of normally distributed data were conducted by Student's *t* test (with Welch's correction in the case of unequal variance) for single comparisons and ANOVA followed by Tukey's test for multiple comparisons. For non-normally distributed data, the Mann–Whitney *U* test and Kruskal-Wallis test followed by Dunn's multiple comparisons tests were used for single and multiple comparisons, respectively. Paired analysis of non-normally distributed data was conducted using Wilcoxon's matched-pairs signed rank test. One-dimensional Pearson correlation coefficients (*r*) were used to compare intensity levels and neurotransmitter release probability. ANCOVA test was performed on all regression lines to determine if slopes were significantly different. Reported values are mean ± SEM. Sample size, statistical test, and *p* values for each comparison are

reported in Table S1.

ACKNOWLEDGEMENTS

We thank the Developmental Studies Hybridoma Bank, the Bloomington *Drosophila* Stock Center, Ehd Isacoff (UC Berkeley), and Stephan Sigrist (Freie Universität Berlin) for providing antibodies and fly stocks. We are grateful to Joel Hirsch (Tel Aviv University) for consultations on tagging Ca-β, Nicholas Deakin (Nikon) for guidance on STORM imaging, the Heckmann lab (University of Würzburg) for guidance on STORM image analysis pipelines, and Liana Lewis for her assistance with image analysis. We thank Rajan Thakur and the members of the O'Connor-Giles lab for thoughtful discussions and comments on the manuscript. This work was supported by grants from the National Institute of Neurological Disorders and Stroke, National Institutes of Health to K.M.O.G (R01NS078179) and Audrey Medeiros (F31NS122424), Brown Neuroscience Graduate Program training grant T32 MH020068, and funds from the Brown University Carney Institute for Brain Science.

REFERENCES

Akbergenova, Y., Cunningham, K.L., Zhang, Y.V., Weiss, S., and Littleton, J.T. (2018). Characterization of developmental and molecular factors underlying release heterogeneity at Drosophila synapses. eLife *7*. 10.7554/elife.38268.

Aldahabi, M., Balint, F., Holderith, N., Lorincz, A., Reva, M., and Nusser, Z. (2022). Different priming states of synaptic vesicles underlie distinct release probabilities at hippocampal excitatory synapses. Neuron *110*, 4144-4161 e4147. 10.1016/j.neuron.2022.09.035.

Aponte-Santiago, N.A., and Littleton, J.T. (2020). Synaptic Properties and Plasticity Mechanisms of Invertebrate Tonic and Phasic Neurons. Front Physiol *11*, 611982. 10.3389/fphys.2020.611982.

Aponte-Santiago, N.A., Ormerod, K.G., Akbergenova, Y., and Littleton, J.T. (2020). Synaptic Plasticity Induced by Differential Manipulation of Tonic and Phasic Motoneurons in Drosophila. The Journal of neuroscience : the official journal of the Society for Neuroscience *40*, 6270-6288. 10.1523/JNEUROSCI.0925-20.2020.

Ariel, P., Hoppa, M.B., and Ryan, T.A. (2012). Intrinsic variability in Pv, RRP size, Ca(2+) channel repertoire, and presynaptic potentiation in individual synaptic boutons. Front Synaptic Neurosci *4*, 9. 10.3389/fnsyn.2012.00009.

Atwood, H.L., and Karunanithi, S. (2002). Diversification of synaptic strength: presynaptic elements. Nat Rev Neurosci *3*, 497-516. 10.1038/nrn876.

Bauer, C.S., Tran-Van-Minh, A., Kadurin, I., and Dolphin, A.C. (2010). A new look at calcium channel alpha2delta subunits. Curr Opin Neurobiol *20*, 563-571. 10.1016/j.conb.2010.05.007.

Bikbaev, A., Ciuraszkiewicz-Wojciech, A., Heck, J., Klatt, O., Freund, R., Mitlohner, J., Enrile Lacalle, S., Sun, M., Repetto, D., Frischknecht, R., et al. (2020). Auxiliary alpha2delta1 and alpha2delta3 Subunits of Calcium Channels Drive Excitatory and Inhibitory Neuronal Network Development. The Journal of neuroscience : the official journal of the Society for Neuroscience *40*, 4824-4841. 10.1523/JNEUROSCI.1707-19.2020.

Bohme, M.A., Beis, C., Reddy-Alla, S., Reynolds, E., Mampell, M.M., Grasskamp, A.T., Lutzkendorf, J., Bergeron, D.D., Driller, J.H., Babikir, H., et al. (2016). Active zone scaffolds differentially accumulate Unc13 isoforms to tune Ca(2+) channel-vesicle coupling. Nature neuroscience *19*, 1311-1320. 10.1038/nn.4364.

Bohme, M.A., McCarthy, A.W., Grasskamp, A.T., Beuschel, C.B., Goel, P., Jusyte, M., Laber, D., Huang, S., Rey, U., Petzoldt, A.G., et al. (2019). Rapid active zone remodeling consolidates presynaptic potentiation. Nat Commun *10*, 1085. 10.1038/s41467-019-08977-6.

Branco, T., and Staras, K. (2009). The probability of neurotransmitter release: variability and feedback control at single synapses. Nat Rev Neurosci *10*, 373-383. 10.1038/nrn2634.

Bruckner, J.J., Zhan, H., Gratz, S.J., Rao, M., Ukken, F., Zilberg, G., and O'Connor-Giles, K.M. (2017). Fife organizes synaptic vesicles and calcium channels for high-probability neurotransmitter release. The Journal of cell biology *216*, 231-246. 10.1083/jcb.201601098.

Campiglio, M., and Flucher, B.E. (2015). The Role of Auxiliary Subunits for the Functional Diversity of Voltage-Gated Calcium Channels. Journal of Cellular Physiology *230*, 2019-2031. 10.1002/jcp.24998.

Cassidy, J.S., Ferron, L., Kadurin, I., Pratt, W.S., and Dolphin, A.C. (2014). Functional exofacially tagged N-type calcium channels elucidate the interaction with auxiliary alpha2delta-1 subunits. Proc Natl Acad Sci U S A *111*, 8979-8984. 10.1073/pnas.1403731111.

Chen, Z., Das, B., Nakamura, Y., DiGregorio, D.A., and Young, S.M., Jr. (2015). Ca2+ channel to synaptic vesicle distance accounts for the readily releasable pool kinetics at a functionally mature auditory synapse. The Journal of neuroscience : the official journal of the Society for Neuroscience *35*, 2083-2100. 10.1523/JNEUROSCI.2753-14.2015.

Cunningham, K.L., Sauvola, C.W., Tavana, S., and Littleton, J.T. (2022). Regulation of presynaptic Ca(2+) channel abundance at active zones through a balance of delivery and turnover. Elife *11*. 10.7554/eLife.78648.

Dai, Y., Taru, H., Deken, S.L., Grill, B., Ackley, B., Nonet, M.L., and Jin, Y. (2006). SYD-2 Liprin-alpha organizes presynaptic active zone formation through ELKS. Nature neuroscience *9*, 1479-1487. 10.1038/nn1808.

Dannhauser, S., Mrestani, A., Gundelach, F., Pauli, M., Komma, F., Kollmannsberger, P., Sauer, M., Heckmann, M., and Paul, M.M. (2022). Endogenous tagging of Unc-13 reveals nanoscale reorganization at active zones during presynaptic homeostatic potentiation. Front Cell Neurosci *16*, 1074304. 10.3389/fncel.2022.1074304.

Davis, G.W., and Muller, M. (2015). Homeostatic control of presynaptic neurotransmitter release. Annu Rev Physiol *77*, 251-270. 10.1146/annurev-physiol-021014-071740.

Dickman, D.K., Kurshan, P.T., and Schwarz, T.L. (2008). Mutations in a Drosophila alpha2delta voltage-gated calcium channel subunit reveal a crucial synaptic function. The Journal of neuroscience : the official journal of the Society for Neuroscience *28*, 31-38. 10.1523/JNEUROSCI.4498-07.2008.

Dolphin, A.C. (2018). Voltage-gated calcium channel alpha (2)delta subunits: an assessment of proposed novel roles. F1000Res *7*. 10.12688/f1000research.16104.1.

Dolphin, A.C., and Lee, A. (2020). Presynaptic calcium channels: specialized control of synaptic neurotransmitter release. Nat Rev Neurosci *21*, 213-229. 10.1038/s41583-020-0278-2.

Dong, W., Radulovic, T., Goral, R.O., Thomas, C., Suarez Montesinos, M., Guerrero-Given, D., Hagiwara, A., Putzke, T., Hida, Y., Abe, M., et al. (2018). CAST/ELKS Proteins Control Voltage-Gated Ca(2+) Channel Density and Synaptic Release Probability at a Mammalian Central Synapse. Cell Rep *24*, 284-293 e286. 10.1016/j.celrep.2018.06.024.

Eggermann, E., Bucurenciu, I., Goswami, S.P., and Jonas, P. (2011). Nanodomain coupling between Ca(2)(+) channels and sensors of exocytosis at fast mammalian synapses. Nat Rev Neurosci *13*, 7-21. 10.1038/nrn3125.

Ehmann, N., Van De Linde, S., Alon, A., Ljaschenko, D., Keung, X.Z., Holm, T., Rings, A., Diantonio, A., Hallermann, S., Ashery, U., et al. (2014). Quantitative super-resolution imaging of Bruchpilot distinguishes active zone states. Nature Communications *5*. 10.1038/ncomms5650.

Fedchyshyn, M.J., and Wang, L.Y. (2005). Developmental transformation of the release modality at the calyx of Held synapse. The Journal of neuroscience : the official journal of the Society for Neuroscience *25*, 4131-4140. 10.1523/JNEUROSCI.0350-05.2005.

Fekete, A., Nakamura, Y., Yang, Y.M., Herlitze, S., Mark, M.D., DiGregorio, D.A., and Wang, L.Y. (2019). Underpinning heterogeneity in synaptic transmission by presynaptic ensembles of distinct morphological modules. Nat Commun *10*, 826. 10.1038/s41467-019-08452-2.

Fouquet, W., Owald, D., Wichmann, C., Mertel, S., Depner, H., Dyba, M., Hallermann, S., Kittel, R.J., Eimer, S., and Sigrist, S.J. (2009a). Maturation of active zone assembly by Drosophila Bruchpilot. The Journal of cell biology *186*, 129-145. 10.1083/jcb.200812150.

Fouquet, W., Owald, D., Wichmann, C., Mertel, S., Depner, H., Dyba, M., Hallermann, S., Kittel, R.J., Eimer, S., and Sigrist, S.J. (2009b). Maturation of active zone assembly by Drosophila Bruchpilot. Journal of Cell Biology *186*, 129-145. 10.1083/jcb.200812150.

Frank, C.A. (2014). Homeostatic plasticity at the Drosophila neuromuscular junction. Neuropharmacology *78*, 63-74. 10.1016/j.neuropharm.2013.06.015.

Frank, C.A., Kennedy, M.J., Goold, C.P., Marek, K.W., and Davis, G.W. (2006). Mechanisms underlying the rapid induction and sustained expression of synaptic homeostasis. Neuron *52*, 663-677. 10.1016/j.neuron.2006.09.029.

Früh, S.M., Matti, U., Spycher, P.R., Rubini, M., Lickert, S., Schlichthaerle, T., Jungmann, R., Vogel, V., Ries, J., and Schoen, I. (2021). Site-Specifically-Labeled Antibodies for Super-Resolution Microscopy Reveal In Situ Linkage Errors. ACS Nano *15*, 12161-12170. 10.1021/acsnano.1c03677.

Fulterer, A., Andlauer, T.F.M., Ender, A., Maglione, M., Eyring, K., Woitkuhn, J., Lehmann, M., Matkovic-Rachid, T., Geiger, J.R.P., Walter, A.M., et al. (2018). Active Zone Scaffold Protein Ratios Tune Functional Diversity across Brain Synapses. Cell Rep *23*, 1259-1274. 10.1016/j.celrep.2018.03.126.

Genc, O., and Davis, G.W. (2019). Target-wide Induction and Synapse Type-Specific Robustness of Presynaptic Homeostasis. Current biology : CB *29*, 3863-3873 e3862. 10.1016/j.cub.2019.09.036.

Ghelani, T., Escher, M., Thomas, U., Esch, K., Lützkendorf, J., Depner, H., Maglione, M., Parutto, P., Gratz, S., Matkovic-Rachid, T., et al. (2023). Interactive nanocluster compaction of the ELKS scaffold and Cacophony Ca²⁺ channels drives sustained active zone potentiation. Science Advances *9*, eade7804. doi:10.1126/sciadv.ade7804.

Gratz, S.J., Goel, P., Bruckner, J.J., Hernandez, R.X., Khateeb, K., Macleod, G.T., Dickman, D., and O'Connor-Giles, K.M. (2019). Endogenous tagging reveals differential regulation of Ca²⁺ channels at single AZs during presynaptic homeostatic potentiation and depression. The Journal of Neuroscience, 3068-3018. 10.1523/jneurosci.3068-18.2019.

Gratz, S.J., Ukken, F.P., Rubinstein, C.D., Thiede, G., Donohue, L.K., Cummings, A.M., and O'Connor-Giles, K.M. (2014). Highly specific and efficient CRISPR/Cas9-catalyzed homology-directed repair in Drosophila. Genetics *196*, 961-971. 10.1534/genetics.113.160713.

Grimm, J.B., English, B.P., Chen, J., Slaughter, J.P., Zhang, Z., Revyakin, A., Patel, R., Macklin, J.J., Normanno, D., Singer, R.H., et al. (2015). A general method to improve fluorophores for live-cell and single-molecule microscopy. Nat Methods *12*, 244-250, 243 p following 250. 10.1038/nmeth.3256.

Guerrero, G., Reiff, D.F., Agarwal, G., Ball, R.W., Borst, A., Goodman, C.S., and Isacoff, E.Y. (2005). Heterogeneity in synaptic transmission along a Drosophila larval motor axon. Nature neuroscience *8*, 1188-1196. 10.1038/nn1526.

Hallermann, S., Kittel, R.J., Wichmann, C., Weyhersmuller, A., Fouquet, W., Mertel, S., Owald, D., Eimer, S., Depner, H., Schwarzel, M., et al. (2010). Naked dense bodies provoke depression. The Journal of neuroscience : the official journal of the Society for Neuroscience *30*, 14340-14345. 10.1523/JNEUROSCI.2495-10.2010.

Hatt, H., and Smith, D.O. (1976). Non-uniform probabilities of quantal release at the crayfish neuromuscular junction. J Physiol *259*, 395-404. 10.1113/jphysiol.1976.sp011472.

He, K., Han, Y., Li, X., Hernandez, R.X., Riboul, D.V., Feghhi, T., Justs, K.A., Mahneva, O., Perry, S., Macleod, G.T., and Dickman, D. (2022). Physiologic and nanoscale distinctions define glutamatergic synapses in tonic vs phasic neurons. bioRxiv, 2022.2012.2021.521505. 10.1101/2022.12.21.521505.

Heinrich, L., and Ryglewski, S. (2020). Different functions of two putative Drosophila α2δ subunits in the same identified motoneurons. Scientific Reports *10*, 13670. 10.1038/s41598-020-69748-8.

Held, R.G., Liu, C., and Kaeser, P.S. (2016). ELKS controls the pool of readily releasable vesicles at excitatory synapses through its N-terminal coiled-coil domains. Elife *5*. 10.7554/eLife.14862.

Holderith, N., Lorincz, A., Katona, G., Rózsa, B., Kulik, A., Watanabe, M., and Nusser, Z. (2012). Release probability of hippocampal glutamatergic terminals scales with the size of the active zone. Nature neuroscience *15*, 988-997. 10.1038/nn.3137.

Hoover, K.M., Gratz, S.J., Qi, N., Herrmann, K.A., Liu, Y., Perry-Richardson, J.J., Vanderzalm, P.J., O'Connor-Giles, K.M., and Broihier, H.T. (2019). The calcium channel subunit alpha(2)delta-3 organizes synapses via an activity-dependent and autocrine BMP signaling pathway. Nat Commun *10*, 5575. 10.1038/s41467-019-13165-7.

Horn, C., Offen, N., Nystedt, S., Hacker, U., and Wimmer, E.A. (2003). piggyBac-based insertional mutagenesis and enhancer detection as a tool for functional insect genomics. Genetics *163*, 647-661. 10.1093/genetics/163.2.647.

James, T.D., Zwiefelhofer, D.J., and Frank, C.A. (2019). Maintenance of homeostatic plasticity at the Drosophila neuromuscular synapse requires continuous IP(3)-directed signaling. Elife *8*. 10.7554/eLife.39643.

Jetti, S.K., Crane, A.B., Akbergenova, Y., Aponte-Santiago, N.A., Cunningham, K.L., Whittaker, C.A., and Littleton, J.T. (2023). Molecular Logic of Synaptic Diversity Between Drosophila Tonic and Phasic Motoneurons. bioRxiv, 2023.2001.2017.524447. 10.1101/2023.01.17.524447.

Kanamori, T., Kanai, M.I., Dairyo, Y., Yasunaga, K., Morikawa, R.K., and Emoto, K. (2013). Compartmentalized calcium transients trigger dendrite pruning in Drosophila sensory neurons. Science *340*, 1475-1478. 10.1126/science.1234879.

Kawasaki, F., Felling, R., and Ordway, R.W. (2000). A temperature-sensitive paralytic mutant defines a primary synaptic calcium channel in Drosophila. The Journal of neuroscience : the official journal of the Society for Neuroscience *20*, 4885-4889. 10.1523/JNEUROSCI.20-13-04885.2000.

Kittel, R.J., Wichmann, C., Rasse, T.M., Fouquet, W., Schmidt, M., Schmid, A., Wagh, D.A., Pawlu, C., Kellner, R.R., Willig, K.I., et al. (2006). Bruchpilot Promotes Active Zone Assembly, Ca²⁺ Channel Clustering, and Vesicle Release. Science *312*, 1051-1054. doi:10.1126/science.1126308.

Kurdyak, P., Atwood, H.L., Stewart, B.A., and Wu, C.F. (1994). Differential physiology and morphology of motor axons to ventral longitudinal muscles in larval Drosophila. J Comp Neurol *350*, 463-472. 10.1002/cne.903500310.

Kurshan, P.T., Oztan, A., and Schwarz, T.L. (2009). Presynaptic alpha2delta-3 is required for synaptic morphogenesis independent of its Ca2+-channel functions. Nature neuroscience *12*, 1415-1423. 10.1038/nn.2417.

Laghaei, R., Ma, J., Tarr, T.B., Homan, A.E., Kelly, L., Tilvawala, M.S., Vuocolo, B.S., Rajasekaran, H.P., Meriney, S.D., and Dittrich, M. (2018). Transmitter release site organization can predict synaptic function at the neuromuscular junction. J Neurophysiol *119*, 1340-1355. 10.1152/jn.00168.2017.

Lipscombe, D., Andrade, A., and Allen, S.E. (2013). Alternative splicing: functional diversity among voltage-gated calcium channels and behavioral consequences. Biochim Biophys Acta *1828*, 1522-1529. 10.1016/j.bbamem.2012.09.018.

Lipscombe, D., and Lopez Soto, E.J. (2019). Alternative splicing of neuronal genes: new mechanisms and new therapies. Curr Opin Neurobiol *57*, 26-31. 10.1016/j.conb.2018.12.013.

Littleton, J.T., and Ganetzky, B. (2000). Ion Channels and Synaptic Organization. Neuron *26*, 35-43. 10.1016/s0896-6273(00)81135-6.

Liu, C., Bickford, L.S., Held, R.G., Nyitrai, H., Sudhof, T.C., and Kaeser, P.S. (2014). The active zone protein family ELKS supports Ca2+ influx at nerve terminals of inhibitory hippocampal neurons. The Journal of neuroscience : the official journal of the Society for Neuroscience *34*, 12289-12303. 10.1523/JNEUROSCI.0999-14.2014.

Liu, K.S., Siebert, M., Mertel, S., Knoche, E., Wegener, S., Wichmann, C., Matkovic, T., Muhammad, K., Depner, H., Mettke, C., et al. (2011). RIM-binding protein, a central part of the active zone, is essential for neurotransmitter release. Science *334*, 1565-1569. 10.1126/science.1212991.

Liu, S., Hoess, P., and Ries, J. (2022). Super-Resolution Microscopy for Structural Cell Biology. Annu Rev Biophys *51*, 301-326. 10.1146/annurev-biophys-102521-112912.

Lnenicka, G.A., and Keshishian, H. (2000). Identified motor terminals in Drosophila larvae show distinct differences in morphology and physiology. J Neurobiol *43*, 186-197.

Los, G.V., Encell, L.P., McDougall, M.G., Hartzell, D.D., Karassina, N., Zimprich, C., Wood, M.G., Learish, R., Ohana, R.F., Urh, M., et al. (2008). HaloTag: a novel protein labeling technology for cell imaging and protein analysis. ACS Chem Biol *3*, 373-382. 10.1021/cb800025k.

Lu, Z., Chouhan, A.K., Borycz, J.A., Lu, Z., Rossano, A.J., Brain, K.L., Zhou, Y., Meinertzhagen, I.A., and Macleod, G.T. (2016). High-Probability Neurotransmitter Release Sites Represent an Energy-Efficient Design. Current biology : CB *26*, 2562-2571. 10.1016/j.cub.2016.07.032.

Ly , C.V., Yao , C.-K., Verstreken , P., Ohyama , T., and Bellen , H.J. (2008). straightjacket is required for the synaptic stabilization of cacophony, a voltage-gated calcium channel α1 subunit. Journal of Cell Biology *181*, 157-170. 10.1083/jcb.200712152.

Macleod, G.T., Chen, L., Karunanithi, S., Peloquin, J.B., Atwood, H.L., McRory, J.E., Zamponi, G.W., and Charlton, M.P. (2006). The Drosophila cacts2 mutation reduces presynaptic Ca2+ entry and defines an important element in Cav2.1 channel inactivation. Eur J Neurosci *23*, 3230-3244. 10.1111/j.1460-9568.2006.04873.x.

McDonald, N.A., Fetter, R.D., and Shen, K. (2020). Assembly of synaptic active zones requires phase separation of scaffold molecules. Nature *588*, 454-458. 10.1038/s41586-020-2942-0.

Melom, J.E., Akbergenova, Y., Gavornik, J.P., and Littleton, J.T. (2013). Spontaneous and evoked release are independently regulated at individual active zones. The Journal of neuroscience : the official journal of the Society for Neuroscience *33*, 17253-17263. 10.1523/JNEUROSCI.3334-13.2013.

Mrestani, A., Pauli, M., Kollmannsberger, P., Repp, F., Kittel, R.J., Eilers, J., Doose, S., Sauer, M., Sirén, A.-L., Heckmann, M., and Paul, M.M. (2021). Active zone compaction correlates with presynaptic homeostatic potentiation. Cell Reports *37*, 109770. 10.1016/j.celrep.2021.109770.

Muhammad, K., Reddy-Alla, S., Driller, J.H., Schreiner, D., Rey, U., Bohme, M.A., Hollmann, C., Ramesh, N., Depner, H., Lutzkendorf, J., et al. (2015). Presynaptic spinophilin tunes neurexin signalling to control active zone architecture and function. Nat Commun *6*, 8362. 10.1038/ncomms9362.

Muller, C.S., Haupt, A., Bildl, W., Schindler, J., Knaus, H.G., Meissner, M., Rammner, B., Striessnig, J., Flockerzi, V., Fakler, B., and Schulte, U. (2010). Quantitative proteomics of the Cav2 channel nano-environments in the mammalian brain. Proc Natl Acad Sci U S A *107*, 14950-14957. 10.1073/pnas.1005940107.

Nakamura, Y., Harada, H., Kamasawa, N., Matsui, K., Rothman, Jason S., Shigemoto, R., Silver, R.A., DiGregorio, David A., and Takahashi, T. (2015). Nanoscale Distribution of Presynaptic Ca2+ Channels and Its Impact on Vesicular Release during Development. Neuron *85*, 145-158. https://doi.org/10.1016/j.neuron.2014.11.019.

Newman, Z.L., Bakshinskaya, D., Schultz, R., Kenny, S.J., Moon, S., Aghi, K., Stanley, C., Marnani, N., Li, R., Bleier, J., et al. (2022). Determinants of synapse diversity revealed by super-resolution quantal transmission and active zone imaging. Nature Communications *13*, 229. 10.1038/s41467-021-27815-2.

Newman, Z.L., Hoagland, A., Aghi, K., Worden, K., Levy, S.L., Son, J.H., Lee, L.P., and Isacoff, E.Y. (2017). Input-Specific Plasticity and Homeostasis at the Drosophila Larval Neuromuscular Junction. Neuron *93*, 1388-1404 e1310. 10.1016/j.neuron.2017.02.028.

Paez-Segala, M.G., Sun, M.G., Shtengel, G., Viswanathan, S., Baird, M.A., Macklin, J.J., Patel, R., Allen, J.R., Howe, E.S., Piszczek, G., et al. (2015). Fixation-resistant photoactivatable fluorescent proteins for CLEM. Nat Methods *12*, 215-218, 214 p following 218. 10.1038/nmeth.3225.

Peled, E.S., and Isacoff, E.Y. (2011). Optical quantal analysis of synaptic transmission in wild-type and rab3-mutant Drosophila motor axons. Nature neuroscience *14*, 519-526. 10.1038/nn.2767.

Peled, E.S., Newman, Z.L., and Isacoff, E.Y. (2014). Evoked and spontaneous transmission favored by distinct sets of synapses. Current biology : CB *24*, 484-493. 10.1016/j.cub.2014.01.022.

Peng, I.F., and Wu, C.F. (2007). Drosophila cacophony channels: a major mediator of neuronal Ca2+ currents and a trigger for K+ channel homeostatic regulation. The Journal of neuroscience : the official journal of the Society for Neuroscience *27*, 1072-1081. 10.1523/JNEUROSCI.4746-06.2007.

Radulovic, T., Dong, W., Goral, R.O., Thomas, C.I., Veeraraghavan, P., Montesinos, M.S., Guerrero-Given, D., Goff, K., Lubbert, M., Kamasawa, N., et al. (2020). Presynaptic development is controlled by the core active zone proteins CAST/ELKS. J Physiol *598*, 2431-2452. 10.1113/JP279736.

Rebola, N., Reva, M., Kirizs, T., Szoboszlay, M., Lőrincz, A., Moneron, G., Nusser, Z., and Digregorio, D.A. (2019). Distinct Nanoscale Calcium Channel and Synaptic Vesicle Topographies Contribute to the Diversity of Synaptic Function. Neuron *104*, 693-710.e699. 10.1016/j.neuron.2019.08.014.

Reddy-Alla, S., Bohme, M.A., Reynolds, E., Beis, C., Grasskamp, A.T., Mampell, M.M., Maglione, M., Jusyte, M., Rey, U., Babikir, H., et al. (2017). Stable Positioning of Unc13 Restricts Synaptic Vesicle

Fusion to Defined Release Sites to Promote Synchronous Neurotransmission. Neuron *95*, 1350-1364 e1312. 10.1016/j.neuron.2017.08.016.

Reuveny, A., Shnayder, M., Lorber, D., Wang, S., and Volk, T. (2018). M-alpha2/delta promotes myonuclear positioning and association with the sarcoplasmic-reticulum. Development *145*, dev159558. 10.1242/dev.159558.

Sauvola, C.W., Akbergenova, Y., Cunningham, K.L., Aponte-Santiago, N.A., and Littleton, J.T. (2021). The decoy SNARE Tomosyn sets tonic versus phasic release properties and is required for homeostatic synaptic plasticity. eLife *10*, e72841. 10.7554/eLife.72841.

Sheng, J., He, L., Zheng, H., Xue, L., Luo, F., Shin, W., Sun, T., Kuner, T., Yue, D.T., and Wu, L.-G. (2012). Calcium-channel number critically influences synaptic strength and plasticity at the active zone. Nature neuroscience *15*, 998-1006. 10.1038/nn.3129.

Smith, L.A., Wang, X., Peixoto, A.A., Neumann, E.K., Hall, L.M., and Hall, J.C. (1996). A Drosophila calcium channel alpha1 subunit gene maps to a genetic locus associated with behavioral and visual defects. The Journal of neuroscience : the official journal of the Society for Neuroscience *16*, 7868-7879. 10.1523/JNEUROSCI.16-24-07868.1996.

Thomas, G.D. (2000). Effect of dose, molecular size, and binding affinity on uptake of antibodies. Methods Mol Med *25*, 115-132. 10.1385/1-59259-075-6:115.

Tong, X.J., Lopez-Soto, E.J., Li, L., Liu, H., Nedelcu, D., Lipscombe, D., Hu, Z., and Kaplan, J.M. (2017). Retrograde Synaptic Inhibition Is Mediated by alpha-Neurexin Binding to the alpha2delta Subunits of N-Type Calcium Channels. Neuron *95*, 326-340 e325. 10.1016/j.neuron.2017.06.018.

Voigt, A., Freund, R., Heck, J., Missler, M., Obermair, G.J., Thomas, U., and Heine, M. (2016). Dynamic association of calcium channel subunits at the cellular membrane. Neurophotonics *3*, 041809. 10.1117/1.NPh.3.4.041809.

Wang, L.Y., and Augustine, G.J. (2014). Presynaptic nanodomains: a tale of two synapses. Front Cell Neurosci *8*, 455. 10.3389/fncel.2014.00455.

Wang, T., Jones, R.T., Whippen, J.M., and Davis, G.W. (2016). alpha2delta-3 Is Required for Rapid Transsynaptic Homeostatic Signaling. Cell Rep *16*, 2875-2888. 10.1016/j.celrep.2016.08.030.

Weiss, N., and Zamponi, G.W. (2017). Trafficking of neuronal calcium channels. Neuronal Signal *1*, NS20160003. 10.1042/NS20160003.

Weyhersmuller, A., Hallermann, S., Wagner, N., and Eilers, J. (2011). Rapid active zone remodeling during synaptic plasticity. The Journal of neuroscience : the official journal of the Society for Neuroscience *31*, 6041-6052. 10.1523/JNEUROSCI.6698-10.2011.

Yazaki, J., Kawashima, Y., Ogawa, T., Kobayashi, A., Okoshi, M., Watanabe, T., Yoshida, S., Kii, I., Egami, S., Amagai, M., et al. (2019). HaloTag-based conjugation of proteins to barcoding-oligonucleotides. Nucleic Acids Research *48*, e8-e8. 10.1093/nar/gkz1086.

Figure 1

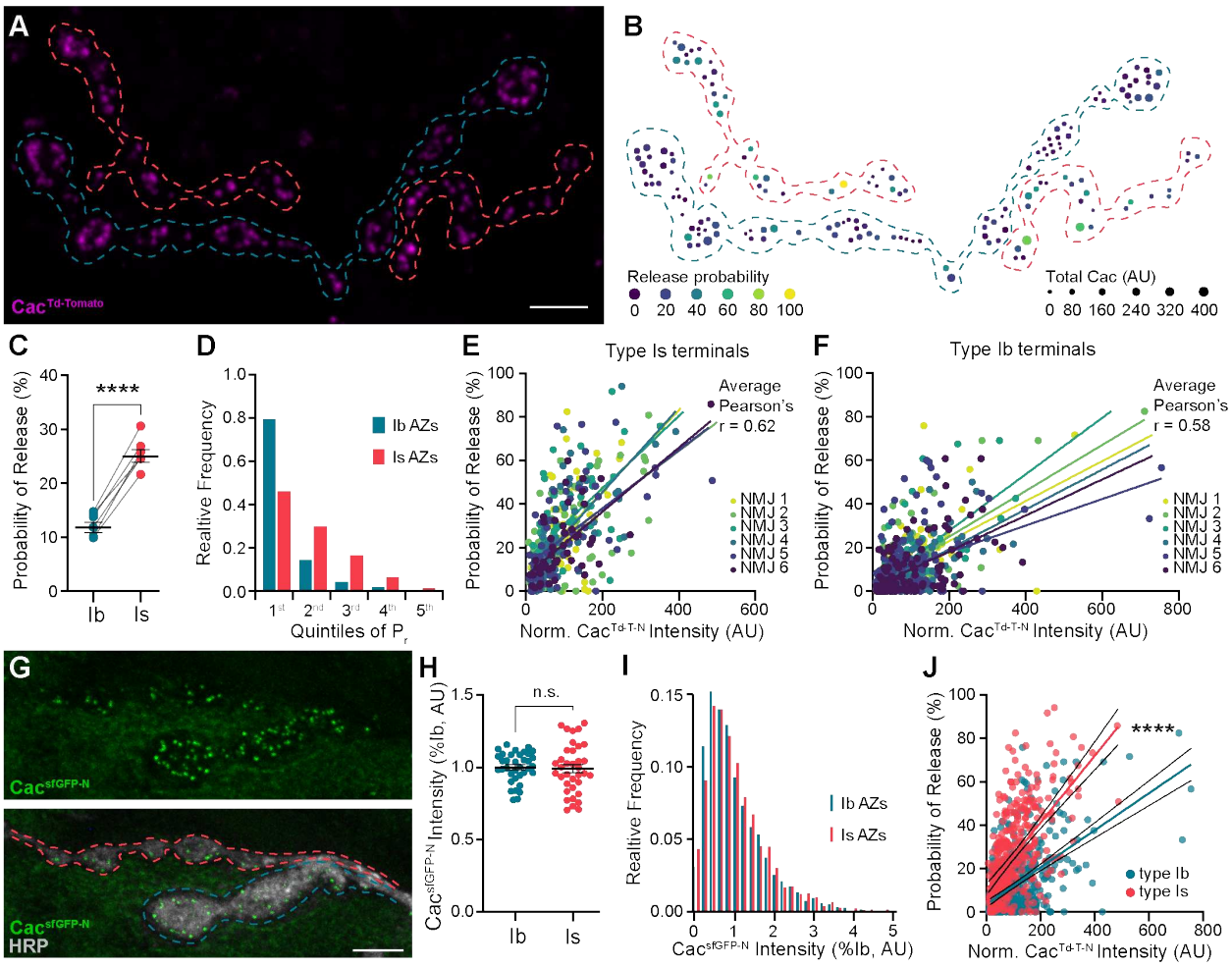

Figure 1. VGCC levels predict P_r within, but not between, synaptic subtypes. (**A**) Representative confocal Z-projection of $Cac^{Td\text{-}Tomato\text{-}N}$ (magenta) with type Ib terminals (blue) and type Is (red) outlined. (**B**) AZ heat map of terminals in A with color indicating release probability (P_r) and size representing sum Cac intensity levels in arbitrary units (AU). (**C**) Average single-AZ probability of release at type Ib and type Is terminals. (**D**) Quintile distribution of single-AZ P_r frequency at type Ib and type Is inputs. (**E, F**) Correlation between normalized $Cac^{Td\text{-}Tomato\text{-}N}$ intensity and P_r at type Is and Ib AZs in the same 6 NMJs. Each dot represents a single AZ and each color corresponds to an individual NMJ with linear regression lines indicated for each NMJ. (**G**) Top, representative confocal Z-projection of $Cac^{sfGFP\text{-}N}$. Bottom, $Cac^{sfGFP\text{-}N}$ in green with HRP marking neuronal membranes in gray. Type Ib (blue) and type Is (red) terminals are outlined. (**H**) Quantification of $Cac^{sfGFP\text{-}N}$ AZ intensity levels at type Ib and type Is terminals. Each data point represents the average normalized single AZ sum intensity for an individual NMJ. (**I**) Distribution of normalized $Cac^{sfGFP\text{-}N}$ intensity from single type Ib and type Is AZs in H (X-axis cutoff at 5.0). (**J**) Correlation between normalized $Cac^{Td\text{-}Tomato\text{-}N}$ and P_r across all Ib and Is AZs combined from E-F with linear regression lines (blue and red, respectively) and 95% confidence intervals (black lines) indicated. All scale bars = 5μm.

Figure 2

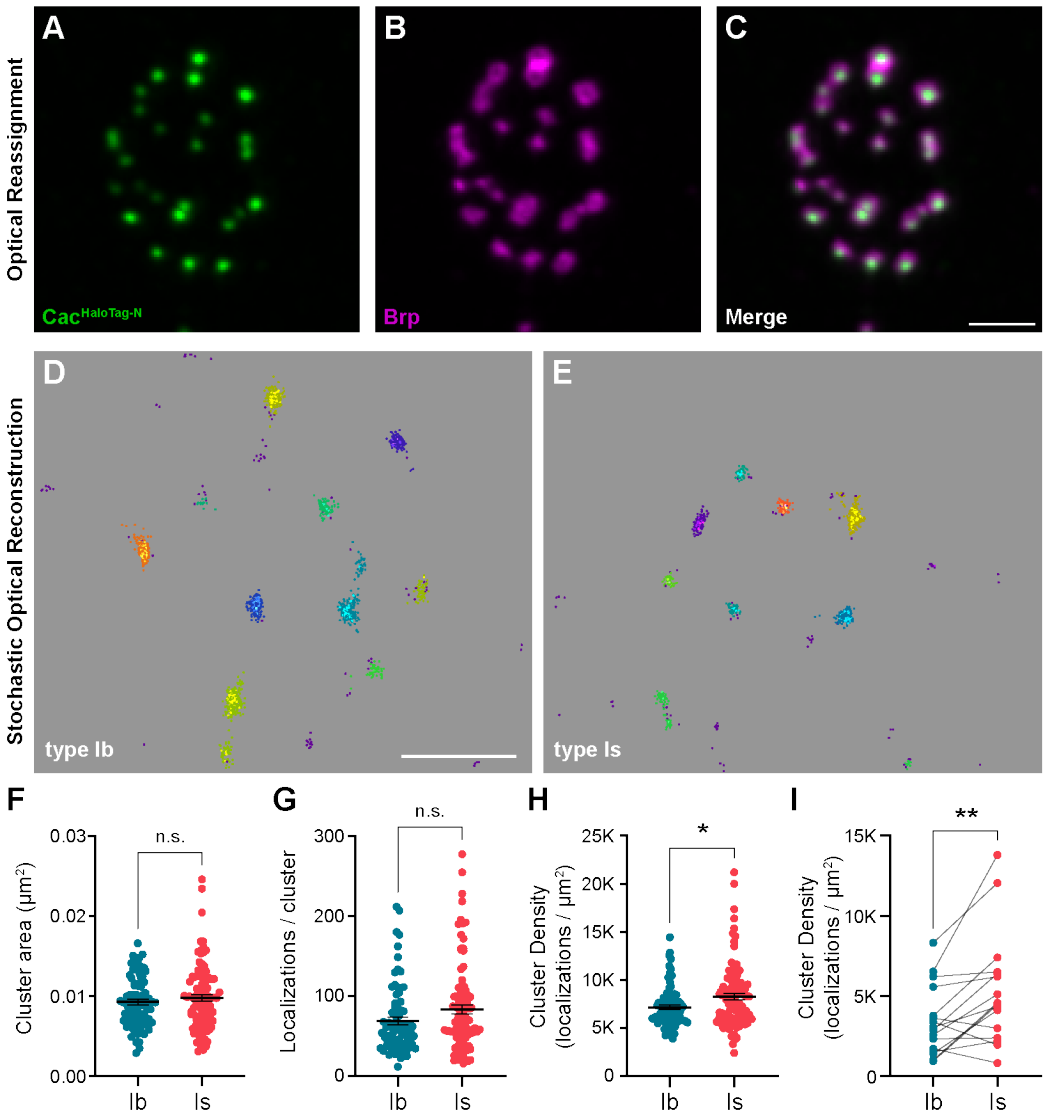

Figure 2. VGCC clusters are more compact at AZs of high-Pr type Is inputs. (**A-C**) Representative SoRa Z-projection of Cac$^{HaloTag-N}$ (green), Brp (magenta), and merge. (**D, E**) Representative boutons of STORM Cac$^{HaloTag-N}$ clusters as identified by DBSCAN at type Ib and type Is boutons as indicated. Each color represents an individual identified cluster with purple scattered dots identifying excluded background signal. (**F**) Quantification of Cac$^{HaloTag-N}$ cluster area at type Ib and type Is AZs. (**G**) Quantification of localizations per cluster at type Ib and type Is boutons. (**H**) Calculated Cac$^{HaloTag-N}$ cluster density at type Ib and Is AZs. For F-H, each data point represents the respective single-cluster measurement averaged over individual boutons. (**I**) A paired analysis of calculated AZ cluster density averaged over individual type Ib and Is inputs at the same NMJ. All scale bars = 1µm.

Figure 3

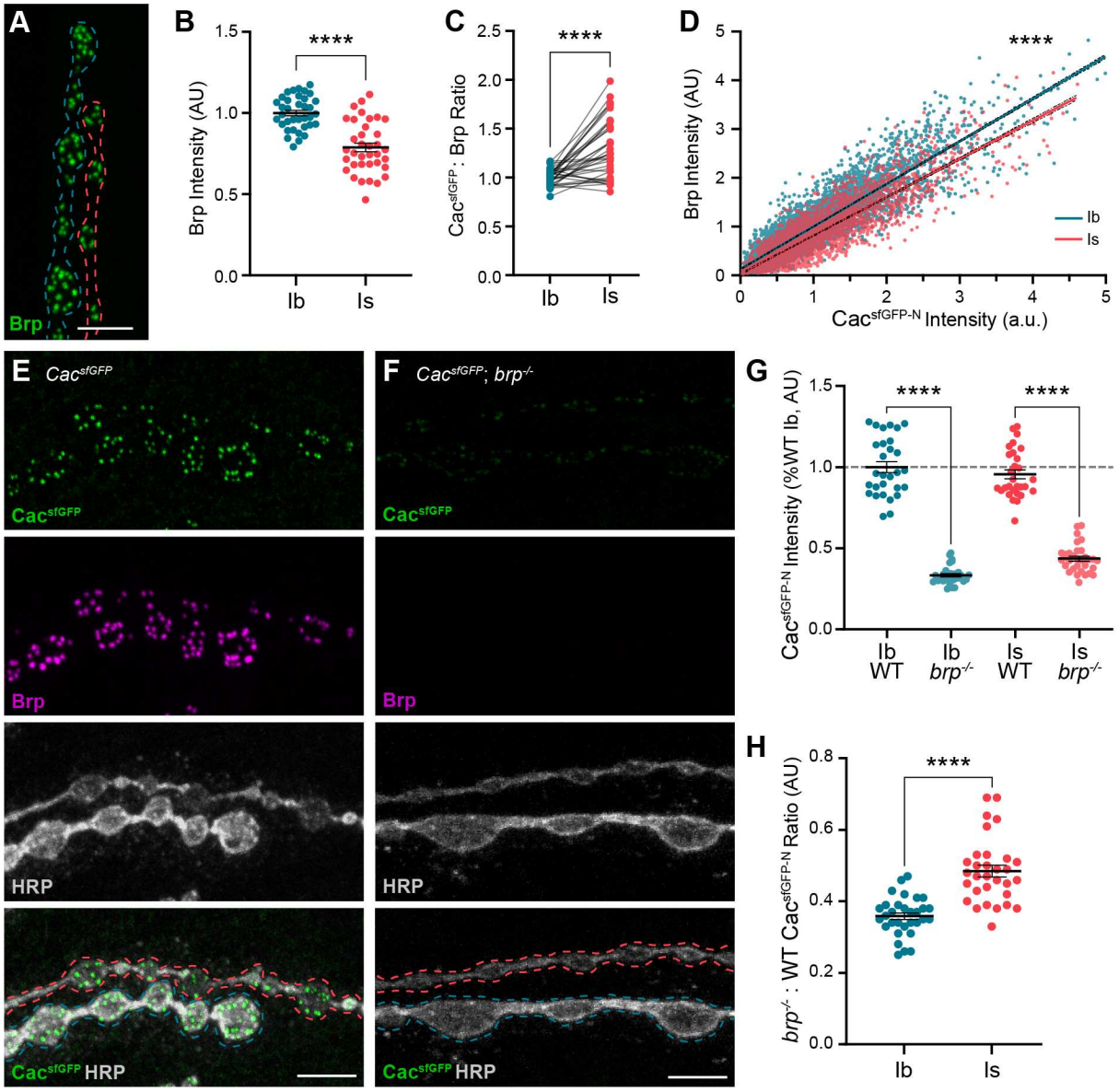

Figure 3. Differences in Bruchpilot levels and function at low- and high-Pr inputs. (**A**) Representative confocal Z-projection of Brp expression at type Ib (blue outline) and type Is (red outline) terminals. (**B**) Quantification of Brp intensity levels at type Ib and type Is AZs. (**C**) Ratio of normalized $Cac^{sfGFP-N}$:Brp levels at type Ib and type Is NMJs. (**D**) Correlation of $Cac^{sfGFP-N}$ and Brp at type Ib and type Is single AZs with linear regression lines (blue and red, respectively) and 95% confidence intervals (black dotted lines) indicated. (**E, F**) Representative confocal Z-projections of $Cac^{sfGFP-N}$ (green), Brp (magenta), HRP (white), and merge at type Ib (blue outline) and Is (red outline) terminals of *$Cac^{sfGFP-N}$* (WT) or *$Cac^{sfGFP-N}$;$brp^{-/-}$* (*$brp^{-/-}$*) animals. (**G**) Quantification of $Cac^{sfGFP-N}$ normalized fluorescence intensity levels at type Ib and type Is AZs of WT vs *$brp^{-/-}$* animals. (**H**) Ratio of $Cac^{sfGFP-N}$ fluorescence intensity levels at type Ib and type Is AZ in *$brp^{-/-}$*:WT. For B and G, each data point represents the normalized single AZ sum intensity measurements averaged over individual NMJs. All scale bars = 5μm.

Figure 4

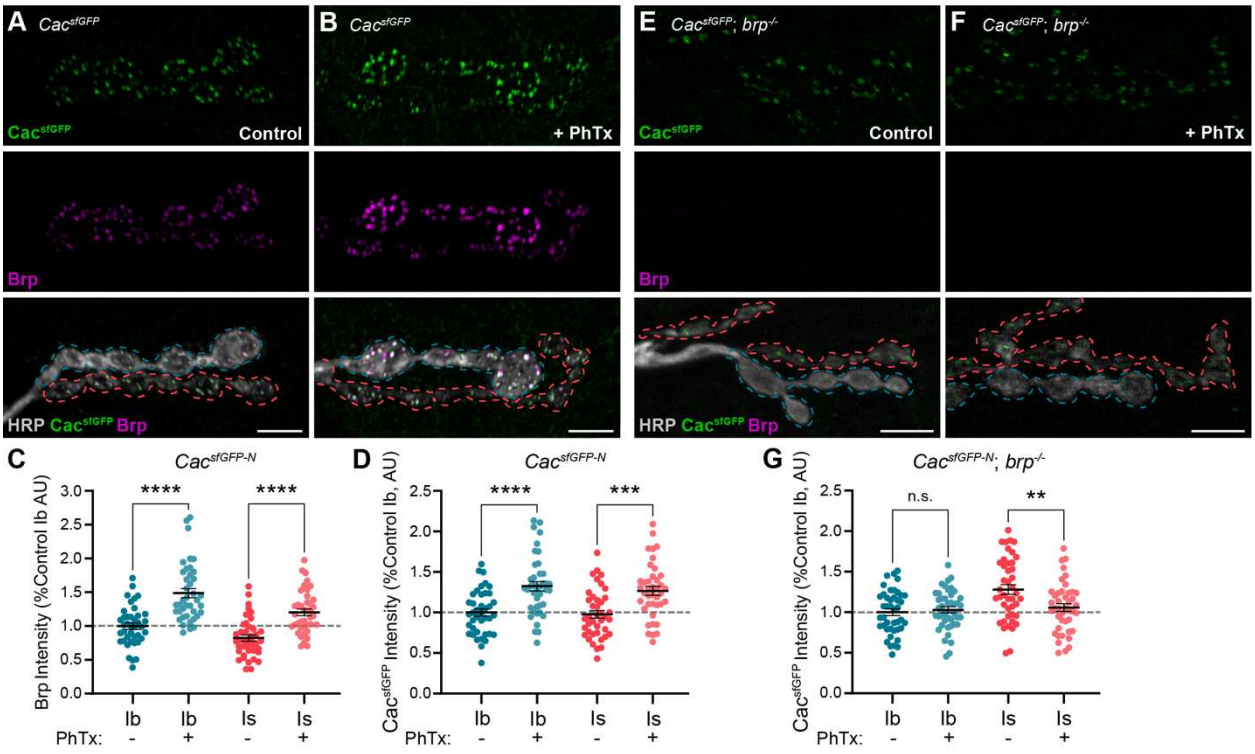

Figure 4. Brp differentially regulates VGCC dynamics at low- and high-Pr inputs during presynaptic homeostatic potentiation. (A, B) Representative confocal Z-projections of Cac$^{sfGFP-N}$ (top, green), Brp (middle, magenta) and merged with HRP (bottom, gray) in untreated and PhTx-treated *Cac$^{sfGFP-N}$* NMJs showing type Ib (blue) and type Is (red) terminals. (**C**) Quantification of Brp fluorescence intensity levels. (**D**) Quantification of Cac$^{sfGFP-N}$ fluorescence intensity levels. (**E, F**) Representative confocal Z-projections of Cac$^{sfGFP-N}$ (top, green), Brp (middle, magenta) and merged with HRP (bottom, gray) in untreated and PhTx-treated *Cac$^{sfGFP-N}$;brp$^{-/-}$* NMJs showing type Ib (blue) and type Is (red) terminals. (**G)** Quantification of Cac$^{sfGFP-N}$ fluorescence intensity levels. For all quantifications, each data point represents normalized single AZ sum intensity measurements averaged over individual NMJs. All scale bars = 5µm.

Figure 5

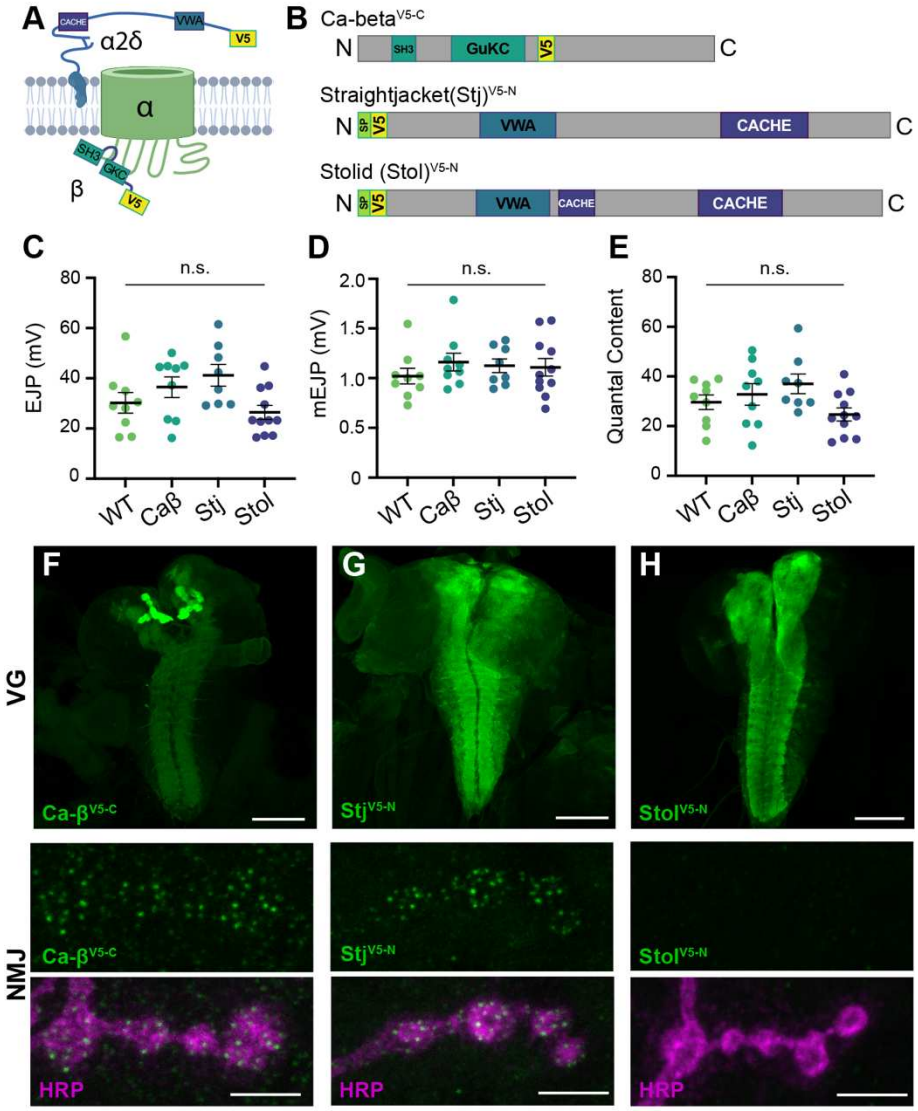

Figure 5. Endogenous tagging of VGCC auxiliary subunits reveals distinct synaptic expression patterns. (**A**) Schematic of Ca^{2+} channel complex with tagged auxiliary subunits (created with BioRender). (**B**) Schematic of Ca-β (isoform PL shown), Stj (isoform PC), and Stolid (isoform H/I) endogenous tag locations. (**C-E**) Quantifications of EJPs, mEJPs, and quantal content for each endogenously tagged line. (**F-H**) Representative confocal Z-projections of auxiliary subunit expression (green) at the larval ventral ganglion (VG, top, scale bars = 100μm), and NMJs co-labeled with anti-HRP (magenta, middle and bottom, scale bars = 5μm).

Figure 6

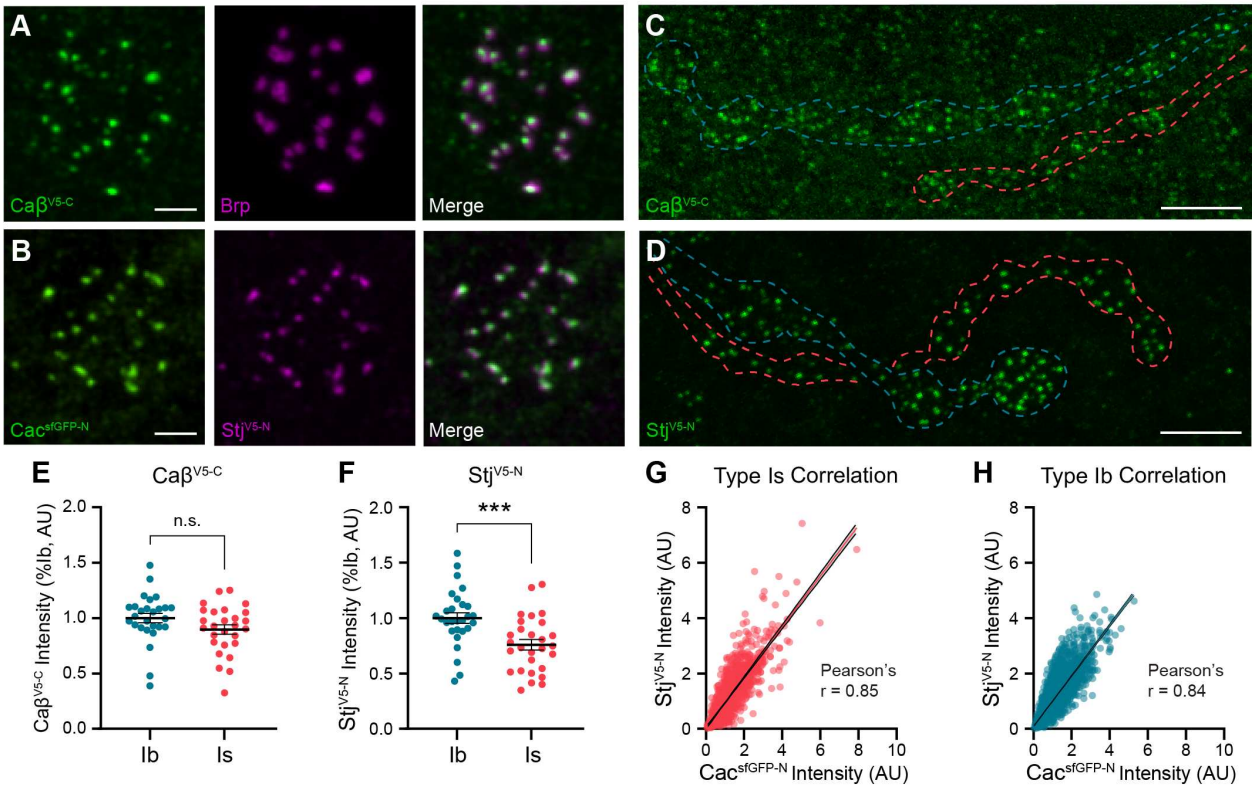

Figure 6. Stj/α2δ-3 levels are lower at AZs of high-P_r type Is inputs. (**A**) Representative SoRa Z-projections of Ca-β$^{V5\text{-}C}$ (green), Brp (magenta) and merge. (**B**) Representative SoRa Z-projections of Cac$^{sfGFP\text{-}N}$ (green), Stj$^{V5\text{-}N}$ (magenta), and merge. Scale bars for A and B = 1μm. (**C, D**) Representative confocal Z-projections of Ca-β$^{V5\text{-}C}$ expression and Stj$^{V5\text{-}N}$ expression at type Ib (blue outline) and type Is (red outline) NMJs. Scale bar = 5μm. (**E, F**) Quantification of Ca-β$^{V5\text{-}C}$ and Stj$^{V5\text{-}N}$ fluorescence intensity levels at type Ib and type Is AZs. Each data point represents normalized single AZ sum intensity measurements averaged over individual NMJs. (**G, H**) Correlation of Cac$^{sfGFP\text{-}N}$ and Stj$^{V5\text{-}N}$ fluorescence intensity levels at type Ib and type Is single AZs with linear regression lines (color lines) and 95% confidence intervals (black lines).

Table S1. Absolute values and statistics. All comparisons, Ns (animals, NMJs, AZs (AZs), and statistical tests used in this study. All values are mean ± SEM.

Figure_Panel	Comparison	Ns	Values/Statistical tests
Fig 1_C	Average P_r in type Ib and type Is	6 animals, 6 NMJs	Ib Average P_r = 12.47 ± 0.88% Is Average P_r = 25.69 ± 1.20% Paired t test, $p < 0.0001$
Fig 1_E	$Cac^{Td\text{-}Tomato\text{-}N}$ to P_r correlation in type Is	6 animals, 6 NMJs	Average type Is Pearson's r = 0.617 ± 0.028
Fig 1_F	$Cac^{Td\text{-}Tomato\text{-}N}$ to P_r correlation in type Ib	6 animals, 6 NMJs	Average type Ib Pearson's r = 0.576 ± 0.035
Fig 1_H	$Cac^{sfGFP\text{-}N}$ levels at type Ib vs type Is	n = 12 animals, 36 NMJs	Type Ib mean: 1.000 ± Type Is mean: 0.991 ± t test, p = 0.78
Fig 1_J	Slopes of $Cac^{Td\text{-}Tomato\text{-}N}$ to P_r correlation at type Ib vs type Is	6 animals, 6 NMJs Type Ib: n = 531 AZs Type Is: n = 365 AZs	Ib Slope = 0.085 ± 0.006 Is Slope = 0.154 ± 0.011 ANCOVA test, $p < 0.0001$
Fig 2_F	$Cac^{HaloTag\text{-}N}$ cluster area in type Ib and type Is	5 animals, 14 NMJs Type Ib: n = 80 boutons 5 animals, 19 NMJs Type Is: n = 96 boutons	Type Ib = 0.0093 ± 0.0004 μm^2 Type Is = 0.0098 ± 0.0004 μm^2 Mann-Whitney test, p = 0.5906
Fig 2_G	$Cac^{HaloTag\text{-}N}$ localizations per cluster in type Ib and type Is	5 animals, 14 NMJs Type Ib: n = 80 boutons 5 animals, 19 NMJs Type Is: n = 96 boutons	Type Ib = 69.39 ± 4.76 Type Is = 83.52 ± 5.67 Mann-Whitney test, p = 0.0928
Fig 2_H	$Cac^{HaloTag\text{-}N}$ cluster density in type Ib and type Is	5 animals, 14 NMJs Type Ib: n = 80 boutons 5 animals, 19 NMJs Type Is: n = 96 boutons	Type Ib = 7185 ± 234.7 μm^{-2} Type Is = 8277 ± 342.6 μm^{-2} Mann-Whitney test, p = 0.0278
Fig 2_I	$Cac^{HaloTag\text{-}N}$ cluster	Type Ib: n = 5	Type Ib = 7300 ± 362.2 μm^{-2}

	density per NMJ in type Ib and type Is	animals, 14 NMJs Type Is: n = 5 animals 19 NMJs	Type Is = 8569 ± 584.0 μm^{-2} Wilcoxon test, p = 0.0076
Fig 3_B	Brp levels at type Ib and type Is	n = 12 animals, 36 NMJs	Type Ib mean: 1.00 ± 0.02 Type Is mean: 0.79 ± 0.03 Unpaired T-test, p < 0.0001
Fig 3_C	$Cac^{sfGFP-N}$:Brp ratio at type Ib vs type Is	n = 12 animals, 36 NMJs	Type Ib mean: 1.00 ± 0.01 Type Is mean: 1.30 ± 0.05 Paired T-test, p < 0.0001
Fig 3_D	$Cac^{sfGFP-N}$:Brp correlation	12 animals, 36 NMJs Ib: n = 5349 AZs Is: n = 2625 AZs	Type Ib slope: 0.874 ± 0.005 Type Is slope: 0.787 ± 0.009 ANCOVA, p < 0.0001
Fig 3_G	$Cac^{sfGFP-N}$ levels in type Ib vs Is in WT and *brp*$^{-/-}$	9 animals WT Ib: n = 29 NMJs $brp^{-/-}$ Ib: n = 31 NMJs WT Is: n = 29 NMJs $brp^{-/-}$ Is: n = 31 NMJs	WT Ib mean = 1.00 ± 0.03 $brp^{-/-}$ Ib mean = 0.33 ± 0.01; p < 0.0001 WT Is mean = 0.96 ± 0.03 $brp^{-/-}$ Is mean = 0.44 ± 0.02; p < 0.0001 Kruskal-Wallis test adjusted p values vs WT
Fig 3_H	*brp*$^{-/-}$:WT ratio of $Cac^{sfGFP-N}$ levels in type Ib vs Is	n = 9 animals, 31 NMJs	Ib ratio = 0.334 ± 0.010 Is ratio = 0.451 ± 0.018 Mann-Whitney test, p < 0.0001
Fig 4_C	Brp levels at *Cac*$^{sfGFP-N}$ type Ib and type Is terminals in control vs PhTx	Control: n = 12 animals, 40 NMJs PhTx: n = 12 animals, 40 NMJs	Control Ib = 1.000 ± 0.044 PhTx Ib = 1.325 ± 0.059; p < 0.0001 Control Is = 0.979 ± 0.047 PhTx Is = 1.268 ± 0.054; p < 0.0001 Kruskal-Wallis test adjusted p values vs Control
Fig 4_D	$Cac^{sfGFP-N}$ levels at *Cac*$^{sfGFP-N}$ type Ib and type Is terminals in control vs PhTx	Control: n = 12 animals, 40 NMJs PhTx: n = 12 animals, 40 NMJs	Control Ib = 1.000 ± 0.047 PhTx Ib = 1.488 ± 0.068; p < 0.0001 Control Is = 0.823 ± 0.046 PhTx Is = 1.203 ± 0.050; p = 0.0006 ANOVA test adjusted p values vs Control
Fig 4_G	$Cac^{sfGFP-N}$ levels at *Cac*$^{sfGFP-N}$; *brp*$^{-/-}$ type Ib and type Is terminals in control	Control: n = 12 animals, 43 NMJs PhTx: n = 12	Control Ib = 1.000 ± 0.041 PhTx Ib = 1.029 ± 0.038; p = 0.9719 Control Is = 1.279 ± 0.059

	vs PhTx	animals, 43 NMJs	PhTx Is = 1.058 ± 0.047; p = 0.0058 ANOVA test adjusted p values vs Control
Fig 5_C	EJPs of endogenously tagged subunits	WT: n = 9 NMJs Stj: n = 8 NMJs Stolid: n = 11 NMJs Ca-β: n = 9 NMJs	WT mean = 30.21 ± 4.09 mV Stj mean = 41.17 ± 4.32 mV; p = 0.14 Stolid mean = 26.44 ± 2.82 mV; p = 0.80 Caβ mean = 36.49 ± 4.09 mV; p = 0.51 ANOVA, adjusted p values vs WT
Fig 5_D	mEJPs of endogenously tagged subunits	WT: n = 9 NMJs Stj: n = 8 NMJs Stolid: n = 11 NMJs Ca-β: n = 9 NMJs	WT mean = 1.02 ± 0.08 mV Stj mean = 1.12 ± 0.07 mV; p = 0.74 Stolid mean = 1.11 ± 0.09 mV; p = 0.78 Caβ mean = 1.16 ± 0.09 mV; p = 0.51 ANOVA, adjusted p values vs WT
Fig 5_E	QC of endogenously tagged subunits	WT: n = 9 NMJs Stj: n = 8 NMJs Stolid: n = 11 NMJs Ca-β: n = 9 NMJs	WT mean = 29.63 ± 2.96 Stj mean = 27.02 ± 3.93; p = 0.34 Stolid mean = 24.73 ± 2.63; p = 0.60 Caβ mean = 32.79 ± 4.34; p = 0.86 ANOVA, adjusted p values vs WT
Fig 6_E	Ca-β$^{V5\text{-}C}$ levels at type Ib vs type Is	n = 11 animals, 27 NMJs	Type Ib mean: 1.00 ± 0.04 Type Is mean: 0.90 ± 0.04 Mann-Whitney Test, p = 0.06
Fig 6_F	Stj$^{V5\text{-}N}$ levels at type Ib vs type Is	n = 9 animals, 28 NMJs	Type Ib mean: 1.00 ± 0.05 Type Is mean: 0.76 ± 0.05 Unpaired t test, p = 0.0008
Fig 6_G, H	Cac$^{sfGFP\text{-}N}$:Stj$^{V5\text{-}N}$ correlation	5 animals, 22 NMJs Ib: n = 4012 AZs Is: n = 2211 AZs	Type Ib slope: 0.912 ± 0.009 Type Is slope: 0.914 ± 0.012 ANCOVA, p = 0.90

Table S2. Imaging details. This table contains detailed information on how each protein was labeled and visualized using live and fixed confocal microscopy and STORM imaging. All secondary antibodies were incubated at RT for 2 hours at a concentration of 1:500.

Imaging Method	Protein	Genetic line	Imaging Reagents	Sample processing
Confocal	Cac	$Cac^{sfGFP-N}$ (Gratz et al., 2019)	anti-GFP AF488 conjugate (ThermoFisher-RRID:AB_221477)	Fix: Bouins or 4% PFA Staining: 1:500, 2 hours at RT
Confocal	Stj	Stj^{V5-N} (this study)	*Primary:* anti-V5 monoclonal (ThermoFisher-RRID:AB_2556564) *Secondary:* Goat anti-Mouse IgG Highly Cross-Adsorbed AF488 (ThermoFisher-RRID:AB_2534088)	Fix: Methanol Primary staining: 1:500, overnight at 4°C *Note, best in 488 channel
Confocal	Stolid	$Stolid^{V5-N}$ (this study)	*Primary:* anti-V5 monoclonal (ThermoFisher-RRID:AB_2556564) *Secondary:* Goat anti-Mouse IgG Highly Cross-Adsorbed AF488 (ThermoFisher-RRID:AB_2534088)	Fix: Bouins Primary staining: 1:500, overnight at 4°C
Confocal	Ca-β	$Ca\text{-}\beta^{C-V5}$ (this study)	*Primary:* anti-V5 monoclonal (ThermoFisher-RRID:AB_2556564) *Secondary:* Goat anti-Mouse IgG Highly Cross-Adsorbed AF488 (ThermoFisher-RRID:AB_2534088)	Fix: Bouins Primary staining: 1:500, overnight at 4°C
Confocal	Brp		*Primary:* anti-Brp (DSHB-RRID:AB_2314866) *Secondary:* Goat anti-Mouse IgG Highly Cross-Adsorbed AF568 (ThermoFisher-RRID:AB_144696)	Fix: Bouins or Methanol Primary staining: 1:100 overnight at 4°C
Confocal	HRP		anti-HRP AF488 conjugate	Fix: Bouins or

			(Jackson ImmunoResearch-RRID:AB_2338965), anti-HRP AF647 conjugate (Jackson ImmunoResearch-RRID:AB_2338967)	Methanol Primary staining: 1:500, 2 hours at RT
Live Imaging	Cac	$Cac^{Td\text{-}Tomato\text{-}N}$ (this study)		
STORM	Cac	$Cac^{HaloTag\text{-}N}$ (this study)	JaneliaFluor 646 HaloTag Ligand (Promega #GA1120)	Live label: 500nM for 20 min in dark box at RT Fix: 4% PFA for 30 min at RT in dark box